PIEZOELECTRIC ENERGY HARVESTING: VORTEX INDUCED VIBRATIONS IN PLANTS, SOAP FILMS, AND ARRAYS OF CYLINDERS

A Thesis
Presented to
The Academic Faculty

by

William B. Hobbs Jr.

In Partial Fulfillment
of the Requirements for the Degree
Master of Mechanical Engineering in the
School of Mechanical Engineering

Georgia Institute of Technology
May 2010

PIEZOELECTRIC ENERGY HARVESTING: VORTEX INDUCED VIBRATIONS IN PLANTS, SOAP FILMS, AND ARRAYS OF CYLINDERS

Approved by:

Professor David Hu, Advisor, Committee Chair
School of Mechanical Engineering
Georgia Institute of Technology

Professor Alexander Alexeev
School of Mechanical Engineering
Georgia Institute of Technology

Professor Silas Alben
School of Mathematics
Georgia Institute of Technology

Date Approved: 29 March 2010

To my beautiful wife,

Lana Beth

for loving and supporting me.

Figure 1: Vortex shedding in a soap film

ACKNOWLEDGEMENTS

There are many people that have helped make this thesis possible. It was directed by my adviser, Dr. David Hu, and input was provided by several other professors, including Dr. Alexander Alexeev and Dr. Silas Alben. A number of graduate students at Georgia Tech provided useful input for this project, including Ben Beck, James Black, Abe Gissen and Nathan Mlot. Help with the soap film setup was provided by Leif Ristroph of Cornell. Several undergraduate students at Georgia Tech helped with this project, including Arfa Butt, Tommy Mark, and Evan Mascianica.

TABLE OF CONTENTS

LIST OF TABLES

LIST OF FIGURES

SUMMARY

The goal of this project was to develop a wind generator that utilizes the collective oscillating motion of multiple piezoelectric devices. These devices would be an alternative to rotating turbine designs for low power generation, for use in applications such as remote power generation. A series of inexpensive devices were developed that harvested energy from vortex shedding, both as independent and cooperative devices. The behavior of single devices was studied, but more interestingly, the way that multiple devices arranged together can increase power output was studied. It was shown that individual devices could harvest more energy if they were placed as specific positions relative to the vortices shed by devices upstream. Through investigating the behavior of these devices, fundamental principles of the phenomenon of vortex induced vibrations were explored. Methods were developed to measure the amplitude and frequency of these vibrations in a wind tunnel, through high speed video and correlations that were found between oscillation and power output from the piezoelectric transducers. Similarly, vortex induced vibrations were explored in an approximation of a two dimensional system in a flowing soap film.

CHAPTER I

INTRODUCTION

Modern technological advances have led to flexible synthetic devices, piezoelectric transducers, which can be incorporated into the structure of a device, allowing it to bend and withstand these forces while also oscillating and converting this mechanical energy into electricity.

Piezoelectric transducers have been used in several designs for fluid flow energy harvesting. Their goal is to generate power, on the scale of microwatts and milliwatts, for small electronic devices such as remote sensors. There have been flag-like devices built, one of which is a piezoelectric eel [52], which is an underwater sheet of piezoelectric polymer that oscillates in the wake of a bluff body. Operating in air, other devices are based on more conventional rotating turbine designs that implement piezoelectrics driven by cam systems [38]. In the category of wheat-like generators is an oscillating blade generator [46], which uses a piezoelectric transducer to connect a steel leaf spring to leaf-like ears.

Each of these designs has drawbacks which are ameliorated in our current design. The piezoelectric eel requires water currents, which limits siting options. Turbine designs have a number of moving and rotating parts, increasing the complexity of manufacture and repair. The oscillating blade generator is most similar to the current design; however, it is not as efficient as it could be, due to the losses in the stalk of the device. While most of these devices are implemented individually, our goal was to design something that would fall into the wheat-like category, being one of the first to be used in large numbers. In these large groups, they would have cooperative interaction, where the contributions of individual devices in the group would be greater than if they were solitary.

Multiple iterations were made on the design of our devices, which changed in orientation and shape, with the reasoning for each change being based on both performance and the way that information about vortex induced vibrations could be gathered. Actual power output per device ranged from 1 to 35 μW, depending on a number of factors. While this is far from power requirements for most electronic devices today, it is believed that there are some limited applications for which

this technology could soon be ready for. And as todays microelectronics become more and more efficient, the viability of this technology becomes closer to realization.

Interesting results were obtained from exploring the influence of flow speed and arrangement on intensity of vibration and power output. These results are presented in the form of dimensionless power as a function of dimensionless spacing, as well as a form of dimensionless velocity. This portion of the work is presented in Chapter 7, which has been submitted for publication in the Journal of Fluids and Structures. Also, a new method was developed for controlling the velocity of a soap film tunnel for a relatively low cost.

1.1 Single Device: Design Testing and Output Characterization

We developed a series of piezoelectric energy harvesting devices and the correlation between their motion and power output was characterized. The device utilized a vertical rigid sail, fixed to a vertically cantilevered piezoelectric transducer. These devices would oscillate in a fixed direction when introduced to wind. Different orientations were tested relative to the wind direction, as were a number of different sail shapes and sizes.

In order to be able to easily measure the motion of the devices, we found a correlation between the velocity of the tip of the stem and the output voltage of the piezo. This significantly reduced the time required for experimentation, as both the physical motion and the electrical performance could be recorded at once, with out the need for video and image processing.

1.2 Single Device: Modeling for Optimization

One project worked on during this thesis was an attempt at creating a 3D geometric model of our energy harvesting device. A method for simulating some aspect of the performance of the design was also to be developed, so that optimization could be performed. This was needed because the level of energy output from prototypes was considered too low to be useful, but it is believed that optimization could lead to a viable product. A highly parametric 3D geometric model was created in MATLAB, and the ability to export the model as STL files for fabrication and validation was incorporated with high success. This format is a stereolithography file, which is a standard input for various types of rapid manufacturing machines. A performance model was created based on the matching of vortex shedding frequency, which is believed to be one of the main causes of oscillation

in this case, and the damped natural frequency of the design. Based on this metric, a basic design space search was performed with limited success by exploring possible configuration combinations. Convergence was not clearly demonstrated, and several problems were found with the approach, but it was still a useful exercise that provided helpful insight into how optimization could continue, and the resulting ability to generate STL files for rapid prototyping would prove very useful if modeled designs needed quick validation.

1.3 Multiple Devices: Flow Visualization

Early in the project, we believed that vortex induced vibrations were significantly contributing to the motion seen in our piezoelectric devices, but more concrete evidence from flow visualization was desired. Several attempts were made a visualization in air using glycerin fog from a common special effects fog machine and a light sheet, but results were never satisfactory. A lack of a powerful light sheet, coupled with the high wind speeds and the density of available fog resulted in very little flow patterns being visualized. Instead of obtaining a more powerful, expensive source for a light sheet, the option of a secondary, dynamically matched system in a soap film tunnel was pursued. A system is developed for testing that is dimensionally matched to a wind tunnel system we present in Chapter 7. Results are presented and discussed, as is a new method we developed for accurately controlling flow speed in a soap film.

1.4 Multiple Devices: Spacing & Flow Velocity Experimentation

The relationship of arrangement and flow speed to power output for a line of four energy harvesting cylinders was investigated. The cylinders oscillated in the flow due to vortex induced vibrations, and energy was captured through piezoelectric transducers embedded in each cylinder. Peak dimensionless power occurs at cylinder spacings of $L/D = 3.3$, which is noteworthy as it is near the critical spacing of $L/D = 3.0$ found by Zdravkovich and Pridden [57]. Also, flow speeds that fixed the frequency ratio, f_s/f_n, at 1.6 resulted in the highest dimensionless power, which differed from the expected result of a peak at resonance. Results of the experiments are presented in several ways. We also visualized flow patterns in a dynamically similar soap film system, which reveals the flow patterns that caused different power outputs.

1.5 Plants

The goal of this project was to develop a wind generator that utilized the collective oscillating motion seen in a field of wheat as an alternative to rotating turbine designs for low power or remote applications. This design looked to wheat and other plants for proven methods of shape optimization for strength and durability, while varying from this design by maximizing the energy captured from the wind.

Recent work has focused on the effects of wind and vortex induced vibrations on plants. Findings in Chapters 7 and 6 made us wonder if plants could be significantly effected by vortex induced vibrations. Preliminary testing has begun to find out if plants subjected to wind flow with a periodic vortex component grow differently than plants subjected to laminar wind or no wind at all.

1.6 Remote Sensing Application

The focus of this project, a novel piezoelectric energy harvesting device, was designed with idea of remote energy generation in mind. Operating on the micro- and milliwatt scale, devices of this type are not necessarily designed to be alternatives to large scale energy generation. Instead, most of these devices, including ours, are designed for applications where batteries or long power cords can be eliminated. In the right application, this can lead to a savings in capital, maintenance, or labor costs.

One application that is a prime candidate for using energy harvesting devices is remote sensing. Environmental and structural sensors are often used in locations where providing power and data connections is not cost effective [39, 49]. Instead, sensors transmit data wirelessly, and power is provided at the individual sensor. To limit power requirements needed for data transmission, sensor networks are often designed where each sensor operates as a node, relaying data along from other sensors. Power often comes from a battery, but there the capacity of the battery must be able to handle the drain from the device long enough that it does not become too time and labor intensive to periodically replace. This situation can be alleviated by generating energy onsite, which is where energy harvesting devices become an option. Through these devices, power is either continuously provided to the sensor electronics, or more often, it is stored in a small battery or capacitor to

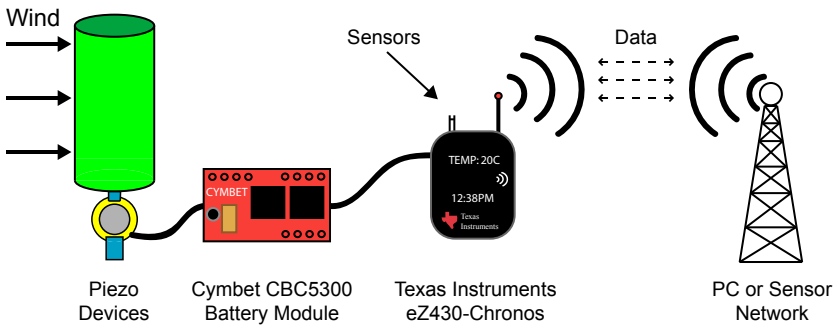

Figure 2: Diagram of possible remote sensing application.

provide more continuous power. This is a viable solution as long as the average power output of the energy harvester is more than the average consumption of the sensor, over periods of time for which the intermediate storage can provide power.

1.6.1 Remote Sensor System Design

A remote sensor system for which our device could potentially provide the required power has been designed. Used as a demonstration for our device, this system would consist of a single node that could wirelessly transmit air temperature and reserve battery voltage level a distance up to 100 m. Data would be recorded on five minute intervals, and transmissions would occur every 24 hours. A diagram of the layout of the system is shown in Figure 2.

The system would be built around the Texas Instruments eZ430-Chronos, a wireless development tool in the form of a wrist watch, which is available as a retail product, and sold as a tool for developers of watches, sports monitoring equipment, and wireless networks. It is built around one of Texas Instruments ultra-low power microcontroller systems, and includes a gigahertz-range wireless transceiver, several sensors, LCD display and is fully reprogrammable. We wrote custom software for one of these watches, allowing it to log temperature data, every five minutes, and automatically transmit the data at a set time every day. A USB radio-frequency (RF) adapter is provided with the kit, which we connected to a PC with a small program scheduled to run at the same time. This allowed us to successfully collect and save the data every 24 hours, while the watch was powered by the original battery. According to the manual for the watch [53], its power requirements in this configuration is an average of about 40 μW, with a peak of 1 mW during RF

transmission.

In order to store energy in a reserve, as output from our devices will drop when wind stops, a battery system was chosen. Cymbet Corporation makes a product, named the EnerChip EH CBC5300, which is an energy harvesting module designed to take an input from a transducer, such as in our system, and charge two built in batteries. The EnerChip has a total capacity of 100 μAh, at a voltage of 3.3 V [9]. This matches the operation voltage range of the watch (3.0–3.6 V) and would provide 2.5–2.75 hours of power to the watch, based on average power requirements of the eZ430-Chronos.

With average power output in the range 2–25 μW for our individual devices, it could be possible for a number of our devices together to provide the power required for this remote sensor demonstration. The number of devices required would depend on the amount of time that wind was available, and addition EnerChip units could be added to increase the storage capacity if needed. And if a more efficient system was needed, the segmented LCD screen on the watch could be deactivated, wether through software or hardware modifications, to decrease the power requirements of the eZ430-Chronos watch. The total cost of this system could be kept around $100, making for a relatively inexpensive demonstration of our devices. The last step required to make an attempt at this demonstration possible would be weatherproofing of our devices, which would not be difficult, especially if the demo was only for a limited time frame.

CHAPTER II

KEY CONCEPTS

Consider cylinders of diameter D, with center-to-center spacing L, in a uniform flow speed of U. The system is characterized by a number of parameters, with the ones of interest being the frequency ratio, f_s/f_n, and the spacing ratio, L/D. The frequency ratio, which is the ratio of the frequency of vortex shedding in the flow around the cylinders to the natural frequency of oscillation of the cylinders, is defined in Equation (1).

$$\frac{f_s}{f_n} = \frac{SU}{\sqrt{E/\rho_c}} \left(\frac{H}{D}\right)^2 \tag{1}$$

Here, S is the Strouhal number, defined in Equations (2), and E, ρ_c, and H are the effective modulus of elasticity, effective density, and height of the cylinder, respectively. These values are outlined in Figure 4.

The spacing ratio L/D is determined by the distance between cylinders in an array, L, and the diameter of the cylinders, D. Illustrations of these dimensions can bee seen in Figure 4 as well. Key dimensionless parameters are shown in Equations (2), including the aforementioned Strouhal number, as well as Reynolds number and mass ratio.

$$Re = \frac{UD}{\nu} \qquad S = \frac{f_s D}{U} \qquad m^* = \frac{H_c D \rho_c}{H_f D \rho_F} \tag{2}$$

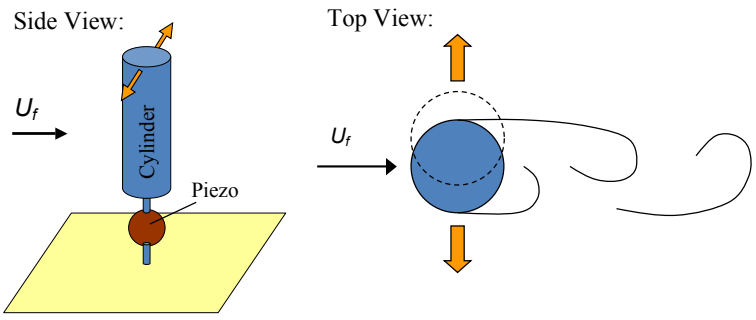

Figure 3: Side and top view of single energy harvesting piezo device. The speed of the incoming fluid is U_f. Instantaneous streamlines are included to demonstrate vortex shedding in the top view.

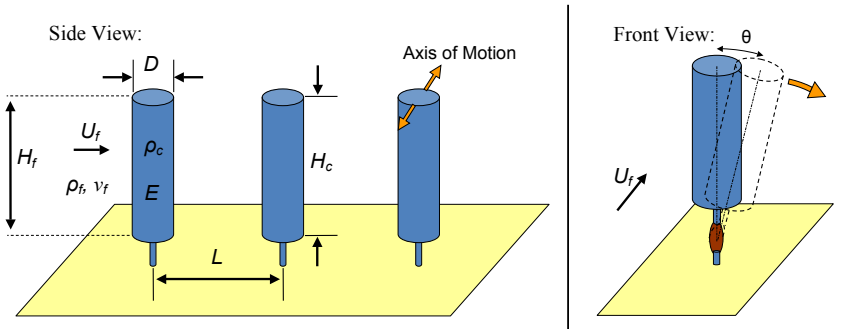

Figure 4: Diagrams showing different system parameters. On the left are key dimensions and values. On the right, a front view. Diagram shows deflection of a single piezo device over half of a period, with incoming flow velocity U_f and a deflection angle of θ.

Here, ν is the kinematic viscosity of the fluid and ρ_f is the density of the fluid, also explained in Figure 4. The velocity, U, in our system was adjusted such that the Reynolds number, Re, ranged from approximately 2000–10000 throughout testing. The relative densities in our system were such that the mass ratio, m^*, ranged from 30–85 for our later designs. It should be noted that

The parameter used to measure the effects of changes in spacing and frequency ratios was the electrical power put out by the piezoelectric devices as the cylinders oscillated in the air flow, as demonstrated by Figure 3 and by the rightmost graphic in Figure 4. Power is described, relative to other parameters, in Equation (3).

$$P = \rho_f U^3 DH \times g\left(Re, \frac{L}{D}, \frac{1}{m^*}, \frac{f_s}{f_n}\right) \tag{3}$$

Here, power is the product of the density of the fluid, the velocity of the fluid cubed, the height of the cylinder, and a function, g, which was based upon dimensional analysis. This function, g, depends on Reynolds number, spacing ratio, the inverse of the mass ratio, and the frequency ratio.

The natural frequency was found experimentally for each design, and stayed in the range of 5–25 Hz. The Strouhal number, S, was assumed to be 0.2 when we were using a circular cross section [6].

For the configuration of our devices, the power output from the piezoelectric transducers is proportional to the angular velocity of cylinders. As the dominant frequency of oscillation is the damped natural frequency of the devices, the power is also proportional to the amplitude of oscillation. Specifically, the rate of change in angle of rotation is linearly proportional to the voltage

output, as shown in Equation (5).

$$\omega = \frac{d\theta}{dt} = cV \tag{5}$$

Here, ω is the angular velocity, or the change in angle θ over time, where θ is illustrated in the rightmost graphic in Figure 4, and c is the correlation constant between the angular velocity and voltage, V, and has units of 1/(seconds-Volts). This constant was found experimentally to be approximately 0.4 (sec-Volts)$^{-1}$, using methods detailed in Section 4.3. This calibration allowed detailed experimental data to be taken by simple recording voltage, forgoing tedious image analysis via high-speed video.

CHAPTER III

PREVIOUS WORK

As this project covered a variety of fields, there is a number of groups in which previous work can be categorized. These include piezoelectric energy harvesting in general, the field of vortex induced vibrations, and research involving soap film tunnels.

3.1 Piezoelectric Energy Harvesting

Piezoelectric energy harvesting is not a new field, but it is seeing much more attention recently as the power requirements of electronics devices are decreasing. Some of the earliest work cited in our project was by V. Hugo Schmidt in the physics department at the University of Montana. He published a paper in 1992 [46], based on work he had been doing as far back at 1982. His paper, *Piezoelectric Energy Conversion in Windmills*, outlined devices he had developed to harvest wind energy. His devices were similar to ours, but moved parallel to the wind, unlike our later devices. Schmidt's design utilized a steel spring in the middle of the devices, were most of the deflection took place. There was also very little further work with his devices. Goldfarb [16] published a paper in 1999, *On the efficiency of electric power generation with piezoelectric ceramics*, which worked with lead zirconate titanate (PZT), which is the same type of piezoelectric material used here. among other things, it was found that in certain configurations, maximum energy could be generated when the piezoelectric transducers were forced at frequencies orders of magnitude below their mechanical resonance frequency. This was encouraging for our work, as our devices were moving on the order of 10 Hz as a whole system, while the resonant frequency of out transducers apart from the whole device was on the order of 1 kHz.

In recent years, S. Priya has done a significant amount of work in the area of piezoelectric energy harvesting. In 2007 Priya published a paper [37] outlining recent developments in and the current state of the field. An excellent introduction to the technology and its potential uses is provided. A discussion on different technologies and specific devices for harvesting energy is also included. Most energy harvesting devices that utilize piezos are designed to collect energy from

mechanical vibration, either on industrial equipment, vehicles, or structures. There is, however, a device developed by Priya [38] that harvests energy from wind. This device, named a "Piezoelectric Windmill," is composed of a simple turbine blade attached to cam mechanisms that flex a collection of piezoelectric bimorphs back and forth as the blade spins in the wind. A theoretical model for the output of this device is provided in another paper [36]. A second generation of this device, capable of 5mW continuous power output, it outlined in a more recent paper by a group including Priya and others [32].

Similar to Priya's overview of piezoelectric energy harvesting technology, a work by Sodano, et al. [48] was also referenced in our work. It provided a similar analysis of state of the art technology, with a specific focus on battery charging, and included real world test results. Similar to the work done by Goldfarb, and of specific interest here, was another paper on energy harvesting using PZT ceramic, also at low frequency, by Platt et al. [35]. Here, an in depth theoretical analysis of energy harvesting performance was provided, based on a number of different parameters.

3.2 Vortex Induced Vibrations

A vast amount of work has been done in the area of vortex induced vibrations (VIV), covering a broad range of aspects in the field. An excellent, thorough review was provided by Willamson and Govardhan [56], covering the entire field, the work that has been done, and questions that still remain. Previous work by Bearman similarly dealt with vortex shedding from externally forced oscillating bodies [3]. A review covering the way vortices interact with downstream bodies is provided by Rockwell [43], which relates to our work as we deal with vibrations caused by objects own wakes and the wake of upstream objects. A reference on the subject of flow induced vibrations, which includes the subfield of VIV, was provided by Blevins [6]. This book was referred to extensively throughout this project, and was found very useful.

Work dealing with the fundamental situation of a single body and its vortex wake included work by Zhou [60] with VIV of a single elastic cylinder. An overview of different flow structures and regimes for a fixed cylinder is provided by Williamson [55]. Gaydon and Rockwell performed work dealing specifically with the forces on a cylinder in a vortex wake [14]. Experiments focused on the phase between the upstream vortex shedding and the oscillation of the cylinder, which was

externally forced. They found that the lateral pressures on the cylinder could be as much as 5 times higher than those for a cylinder similarly forced to oscillate, but without being in a vortex wake. This phenomenon was crucial to our work, as we were investigating how an upstream vortex wake could similarly increase power output. Equally important to our research was the work of Govardhan, Jauvtis and Williamson. Govardhan and Williamson [17] confirmed that an elastically mounted cylinder with mass ratio on the order of 100 will oscillate at a frequency very close to its natural frequency. This was important for our research, as the mass ratios we were dealing with were in the range of 30-80. This meant that for us to increase power output, we were going to have to increase the amplitude of oscillation, as the frequency for a particular design would be essentially fixed. Jautis and Williamson [21] studied the effects of mass ratio on the direction of oscillation relative to the flow. There results were equally important, as they showed that for mass ratios greater than 6, elastic cylinders would oscillate almost completely transverse to the flow, regardless of freedom to move parallel to the flow.

Still regarding single cylinders and VIV, but in a category of its own, was work by Bernistas et al. [5]. Their group is developing a technology named VIVACE (Vortex Induced Vibration for Aquatic Clean Energy) which consists of cylinders which harvest energy from underwater currents. The cylinders are on the order of 1 m long and 0.1 m in diameter, and are coupled to a generator. While there are similarities to our devices, these devices differ from our own most significantly in that they are designed to work independently, where each device is far enough from the next that their wakes do not effect each other. Also of significance is the fact that, due to their underwater nature, the mass ratio at which the VIVACE system operates is on the order of 1, which changes their fundamental behavior. Never the less, this work by Bernistas et al. was valuable in that it was some of the most similar work to our own, and some of the fundamentals behind their work still apply to our project.

Previous work with vortex shedding and VIV can also be placed into another group, where it involves the condition of multiple bodies in the flow in close proximity. This category is where our work would fall, as the interactions of bodies with the wakes of other bodies is a key aspect of our project. Fundamental work, looking at the effects of spacing on the flow around two cylinders in tandem, was performed by Zdravkovich [57, 58]. While this work was with fixed cylinders, it

explored different flow regimes, and the spacings at which they occur, which we discuss in Chapter 7. Using similarly fixed cylinders, Lin et al. studied the effect of spacing on flow structures, and found increasing buffeting of the downstream cylinder as spacing increased. They also found full Karman vortex shedding from the first cylinder at spacings above $L/D = 4$. Work dealing with vortex shedding in a system with two forced cylinders, not elastically supported, was done by Mahir and Rockwell for cylinders in side-by-side [27] and tandem arrangements [26]. A focus was placed on the range of frequency lock-in, where the frequency of vortex shedding is locked to the frequency of oscillation of the cylinder. Relating to our work, they found that the range of frequency lock-in is larger for two cylinders in tandem than for an individual cylinder, which could partially explain higher power output per cylinder for arrays than for individual cylinders. Work has also been done in this area using numerical models, [29] [30].

Our work is different form the majority of the work in the multiple clinder category, however, because much of our work focused on four cylinders. With four cylinders, we sometimes found trends that were not present in just two, or even three cylinders. And where previous work does focus on more than two cylinders, it only looks at vortex shedding from fixed cylinders [20, 19] or the study on VIV is limited to acoustic vibrations in the kilohertz range [61]. Igarashi did some of the earliest work on three, four and five cylinder rows, defining different flow patterns that emerge as spacing and Reynolds number increase. Similar work was later performed by Hetz et al. [18] with a row of five cylinders, proving the existence of vortex shedding in the gaps between cylinder, and predicting that this shedding in arrays of cylinders could lock on to structural vibrations, causing large oscillatory forces.

3.3 Soap Film Tunnels

Soap films were first used for serious 2D fluids experiments by Couder, including experiments with vortex shedding behind oscillating cylinders, similar to the work done here [7, 8], using a stationary horizontal film through which objects were dragged. Interference patterns in reflected light caused by variations in film thickness provided visualization of flow patterns in a close approximation to two dimensional flow [7, 28]. Limitations with Couder's method, however, included limited speed at which experiments could be performed and the lack of steady state flow experimentation. Gharib

et al. [15] later developed a flowing soap film apparatus, where a film was drawn between rigid horizontal rails by a sheet of sprayed water at the end of the rails. This method provided steady state flow, but was difficult so start up and required relatively complicated equipment. Kellay et al. [22] developed a similar flowing soap film apparatus, but unlike Gharib's, it was pulled along by gravity between vertical wires after being started by hand by drawing a squeegee down the wires. This design was further improved upon, as described by Rutgers [45], by adding a nozzle for flow control and using flexible wires run through the nozzle that could be pulled apart at their midsections to create the soap film. This design allowed a film to be started very quickly, and it allowed for flow rate to be adjusted easily, providing soap film velocities of 0–3 m/s.

Beizaie and Gharib [4] published work on soap film fundamentals, including work that was useful here regarding film thickness, surfactant concentration, and flow velocity. Important information on velocity profiles and velocity measurement was provided by another paper by Rutgers [44]. The experimental apparatus used in this project was developed based partially on details published by Zhang et al. [59], where work was done using filaments in a soap film as a model for one dimensional flags in two dimensional wind, and on work done by Ristroph and Zhang [41] with interactions between two such flags.

CHAPTER IV

SINGLE DEVICE: DESIGN TESTING AND OUTPUT CHARACTERIZATION

In this Chapter, we present methods and results for testing of multiple designs for single devices. We go through the process of selecting a piezo transducer for our design, and then test the size, shape and orientation of different designs of the devices. We also work to characterize the relationship between the motion of the devices and their power output, resulting in a reliable correlation.

4.1 Early Design

The earliest testing for this project involved adjustments of the shape, orientation, and composition of our piezoelectric devices. The first iteration of the design consisted of a piezoelectric buzzer, positioned on its edge, with the bottom fixed and the top attached to a sail via a stem. A photograph of one of the first devices is shown in Figure 5. The assembly would be placed in a moving air stream, such that the plane of the sail and the piezo buzzer was perpendicular to the flow. The sail would oscillate forwards and backward relative to the flow, causing the piezo to bend back and forth. This, through the direct piezoelectric effect, would cause the piezo to generate a current through any electric load connected to it.

As a number of devices were to be tested in groups, materials had to be acquired with which numerous identical devises could be built. And, as maximum power output was an end goal, the type of piezo transducer that was used was the first thing to be selected. Tests were carried out on five different piezo transducers, four piezo buzzers intended for use as simple audio speakers, and one bimorph designed for industrial applications. Each piezo was inserted into an assembly much like the one shown in Figure 5, and placed in front of a common box fan. The setup was oriented such that oscillation was perpendicular to the flow. The voltage put out by each piezo across a 100 kΩ resistance was measured for 30 seconds, and the average of the data was taken. Two of the transducers, the bimorph and one of the buzzers from Mouser, were two-sided, and for these transducers output from only one side was measured. The power output, P, for each piezo was

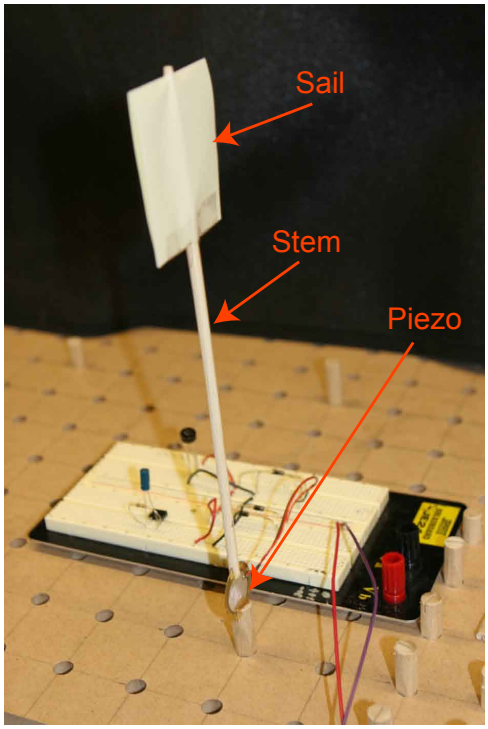

Figure 5: Photograph of first iteration of the piezoelectric device. The sail, stem, and piezoelectric buzzer are labeled. Also included in the image is the peg to which the piezo is attached, the peg board that allows positioning of multiple devices, and a simple rectifying circuit.

Table 1: Comparison of multiple piezoelectric transducers considered for use. Selection was based on highest energy output per cost, based on testing in a particular configuration.

Piezo	Supplier	Part #	Power (uW)	Cost	uW/$1
R	Radio Shack	273-073	3.51	$2.00	1.76
A	Mouser	665-AB4113B	6.96	$1.38/2	10.08
B	Mouser	655-AB2720B	4.35	$1.21	3.60
C	Mouser	665-KB1-3526	3.60	$1.21	2.97
Bimorph	APC Int.	40-1010 (APC)	6.60	$11.27/2	1.17

then calculated from the voltage, V, and resistance, R, using Equation (4).

$$P = \frac{V^2}{R} \tag{4}$$

The retail cost was then considered for each piezo, which was divided into its average power output. For the case of each of the double sided piezos, the cost was divided by two to account for the additional side. The results of this comparison are shown in Table 1. Based on the metric used, piezo buzzer "A", the double sided buzzer from Mouser, was the clear winner. This piezo was also the largest of the buzzers, with a diameter of ∼4 cm, making it easier to work with.

Multiple devices were then built according to the design shown in Figure 6. Larger sails were used to make two-dimensional approximations more accurate, and they were found to increase the power output about 10%. Slits were cut into the peg/base and the stem, and these joints were then epoxied to the piezo. Paper sails were attached to the stem with paperclips, which allowed for easy adjustments of height and center of mass, to ensure that each device had similar characteristics.

Shortly after these devices were built, it was discovered that orienting them such that oscillation was perpendicular to the flow, as shown in Figure 7, resulted in a 50–100% increase in power output. This orientation was then used for the remainder of the project, and the reasoning for the power increase was later investigated. The velocity over time of the tip of two of the devices is shown in Figure 8, as a demonstration of the type of motion in the system. The velocity was calculated from the voltage output recorded by an oscilloscope, using methods described in Section 4.3.

4.2 Design Testing

The effect of arrangement of multiple devices was of significant interest. One hope was that relationships could be found between optimal configuration for energy harvesting and the configuration

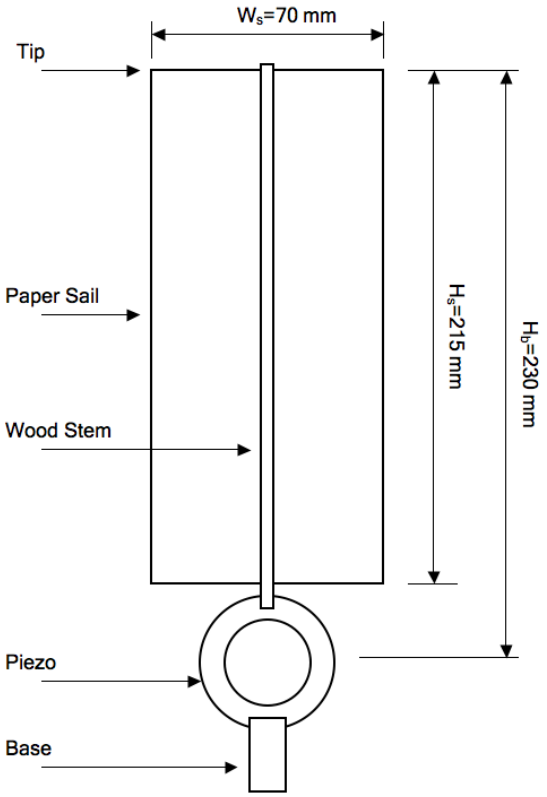

Figure 6: Diagram of second design. The sail area has been increased from the first design (Figure 5) and the orientation relative to the flow has changed, as shown in Figure 7.

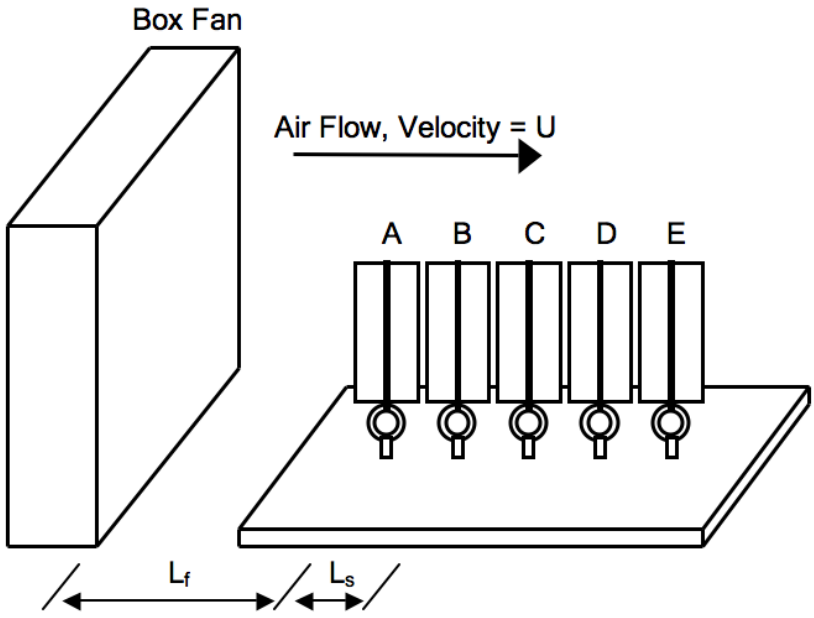

Figure 7: Adjusted orientation of new devices relative to air flow. From the previous design, the orientation has changed by 90 degrees and the size of the sail has increased. Different spacing lengths are highlighted.

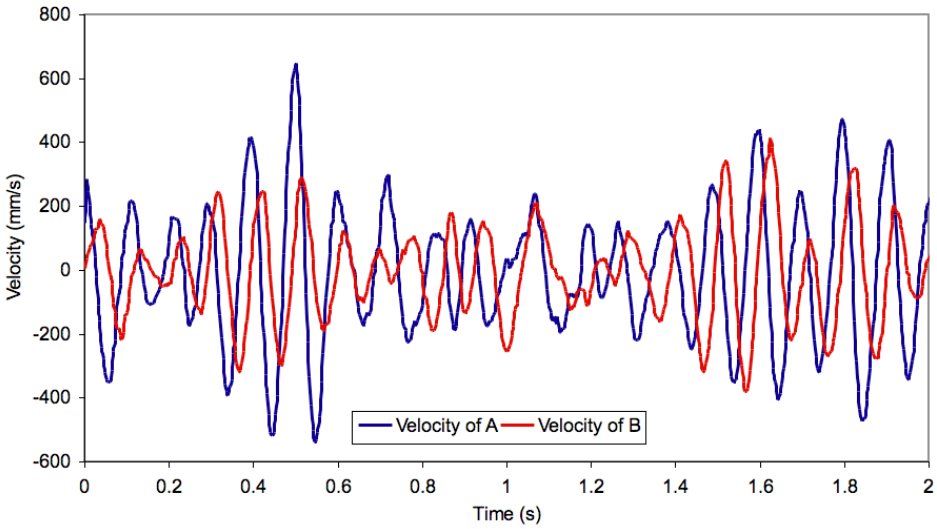

Figure 8: Velocity of two devices over 2 seconds, shown as an example of the behavior of these devices. The positions of devices A and B are as shown in Figure 7.

of organisms in nature that are subject to flow, such as groves trees or schools of fish. As such, a particular design for the individual devices had to be selected before testing could expand into investigating the effects of arrangement. To do this, a single piezo and stem assembly had multiple sails attached, and tests were run with each. The sails were made of corrugated plastic, the type often used for advertising signs, and widths and heights of sails tested ranged from 1.5–4" and 8–14", respectively, with five heights tested and six widths. To reduce the number of tests, a 12" long by 2" wide sail was chosen as the baseline. Heights were then only tested at a width of 2", and widths were only tested at a length of 12". The angle from parallel, where the two planes measured are that of the flow and that of the sail, was also tested at increments from 0 to 90 degrees. The results of the height and width tests are shown in Figure 9, and the results of the angle tests are shown in Figure 10.

For the width test, peak power was found at 2.5" wide (12" long) and for the length tests peak power was found at 14" long (2" wide), which was at the edge of the tested range. For the angle tests, it was clear that orienting the sale parallel to the flow produced the highest output. These tests were carried out in a small wind tunnel, where a box fan was used to pull air into the tunnel. It was found that flow was more laminar when pulling air through the tunnel than by blowing it directly across the devices.

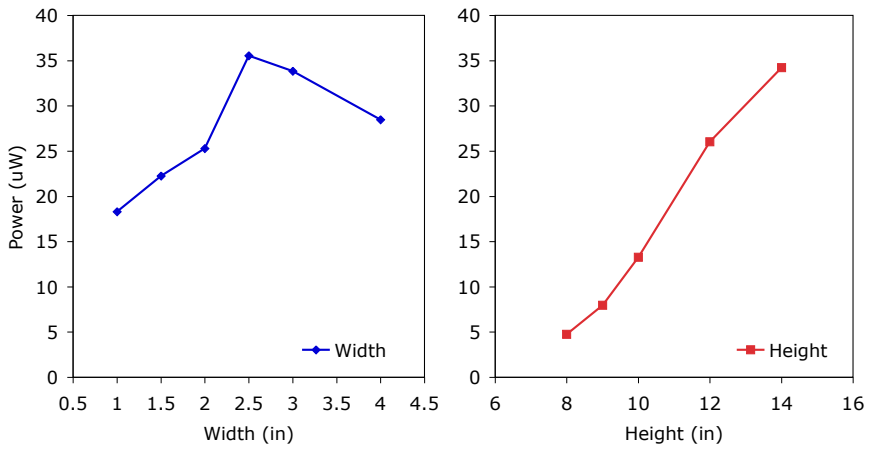

Figure 9: Power as a function of sail width and height. Width tests (left, blue) were performed at a height of 12", and height tests (right, red) were performed at a width of 2". All tests were with a single device in the flow.

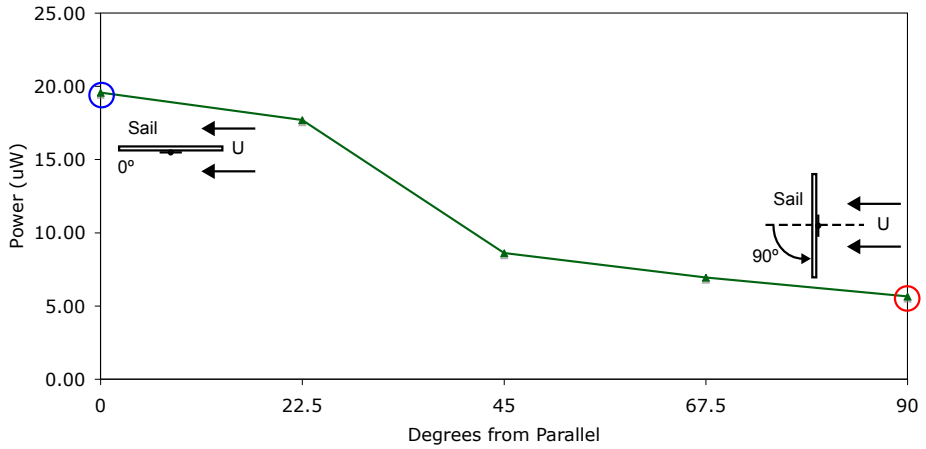

Figure 10: Power as a function of angle with the flow for a 12" long, 2" wide sail. Zero degrees corresponds to the plane of the sail being parallel to the flow, with the direction of oscillation being transverse to the flow.

4.3 Output Characterization

In order to be able to easily measure the motion of the devices, we found a correlation between the velocity of the tip of the stem and the output voltage of the piezo. This was done by filming the tip of the stem after being manually deflected, with a reference image being saved that had an object of known length for size scaling, while simultaneously recording the voltage across a known resistance of a current generated by the piezo. Image processing software was used to determine the position of the tip of the stem over time. This was then converted to angular velocity, using the length of the stem and a small angle approximation, and compared to the voltage. The relationship between the angular velocity, ω, and the voltage, V, is shown in equation (5).

$$\omega = \frac{d\theta}{dt} = cV \tag{5}$$

The relationship between the voltage and the angular velocity was constant, labeled here as c, and it was found experimentally to be approximately 0.4 when the voltage was measured across a resistance of 1 MΩ. After scaling by this constant, a very good fit could be shown between the angular velocity and the voltage, demonstrated in Figure 11. Angular velocity and scaled voltage are plotted together, with values read from the y-axis on the left, and the angle of deflection being shown for reference, with values on the y-axis on the right. The vertical dashed line marks the point in time at which the device was released from static deflection. This further illustrates the point that the voltage is proportional to the derivative of the deflection angle, angular velocity, as the voltage is 90 degrees out of phase with the angle. It is also worth pointing out that as the motion of the piezo devices is periodic and closely resembles a sine wave, the voltage output will always be proportional to the amplitude of oscillation.

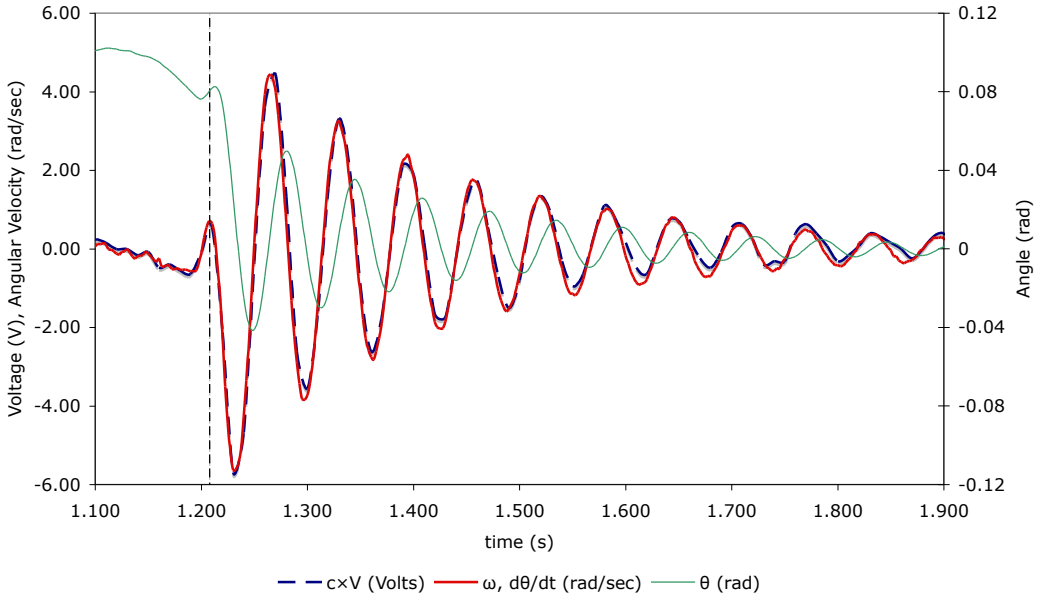

Figure 11: Comparison of angular velocity and scaled voltage from a moving piezo device. These two sets of data are plotted in reference to the left axis, and the angle of deflection is plotted using the right axis.

CHAPTER V

SINGLE DEVICE: MODELING FOR OPTIMIZATION

Throughout this project, modeling the behavior of our devices had been a difficult proposition. The ability to model flow around objects has been around for a long time, but the addition of oscillating object boundaries, such as is the case for this project, significantly increased the complexity. As such, a greatly simplified model was developed to model the behavior of an single device. A book by Robert Blevins, *Flow-Induced Vibrations* [6], was used as a reference for this model. We believed that one of the main causes for oscillation of our devices in wind was oscillating pressure fields caused by vortex shedding around the body. Blevins book contains correlations between the frequency of this shedding and common shapes and the velocities of flow they are exposed to. Similarly, to define the natural damped resonant frequency of the device, this book contained equations to define the damping factors of objects in fluid flow.

This realization that the vibrations in our devices were most likely caused by vortices was an import step in the project, as it was the point at which our design turned from flat sails to three dimensional ones. These would generate larger, more defined vortex wakes, which was hoped to increase power output, and also make analysis easier. Circular and oval cross sections, in particular, would be the easiest to predict the vortex shedding from, and we chose those types of designs as the project moved forward.

The overall approach to this portion of the project was to first take an existing physical prototype and design a new configuration that would incorporate parameters that would control key aspects of the design related to its performance. Based on the current understanding of important variables in the mechanisms of flow induced vibrations, this new design allowed for variable width and depth of the body of the device with respect to fluid flow direction, as well as length and mass. This design was modeled geometrically in 3D in MATLAB. There were then two directions taken from this point in the project. The first objective also to use this 3D geometric model to measure and, possible in the future, optimize efficiency with a performance model. The second objective was

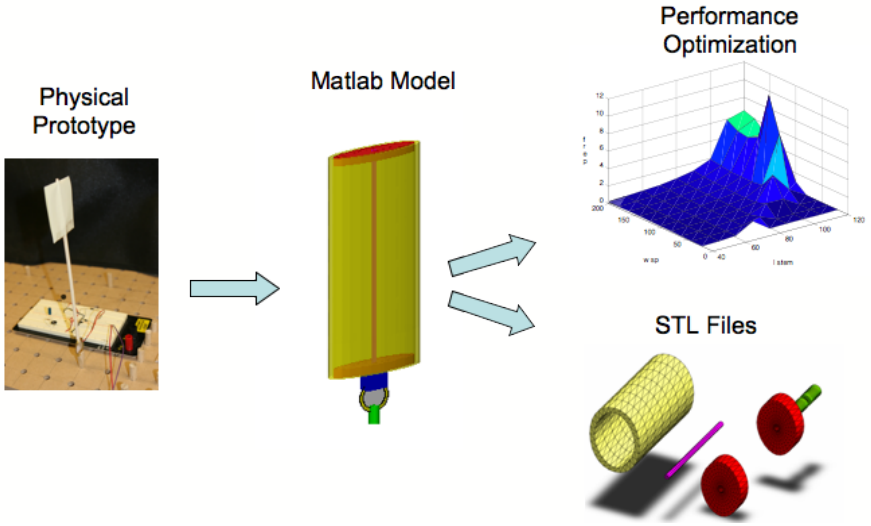

Figure 12: Diagram showing main steps for modeling. A 3D geometric model was developed in MATLAB based on a physical prototype, which was then used for performance evaluation/optimization and conversion to STL file format.

to convert this model to a file format that could be eventually used for rapid prototyping, in this case the STL format was used. This format is a stereolithography file, which is a standard format for rapid prototyping and computer aided manufacturing. A diagram showing these mains steps is shown below as Figure 12.

5.1 Design Parameters

The main input parameters for the geometric and performance models were controlled from the top level as the input of a function that generated the geometric model. The geometric model was fully parameterized, meaning that changes in one part length would result in other lengths being sized automatically to fit. The values that were parameterized included the length of the sail, the width of the spacers, the depth of the spacers, the thickness of the spacers (affecting mass), the thickness of the sail (affecting mass and overall width and depth), and the resolution with which the model was created. Examples of these parts and dimensions are shown in Figure 13.

5.2 Performance Model

For this project, performance was modeled as the closeness of the match between the damped natural frequency of the piezo-wheat and the frequency of vortex shedding in the flow around the

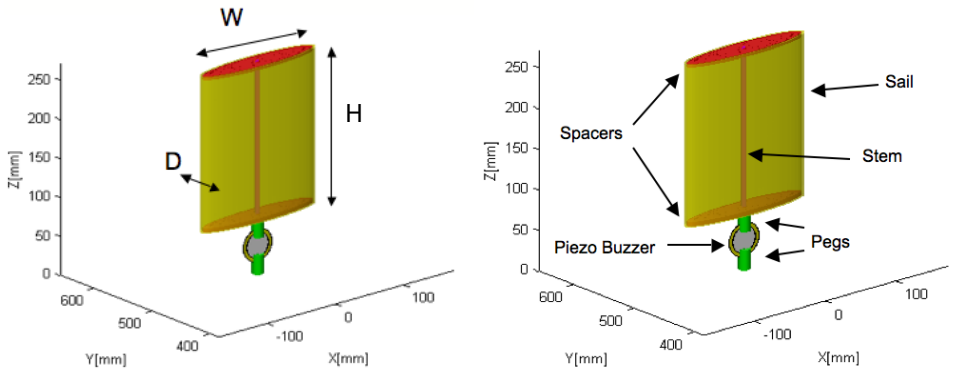

Figure 13: Major dimensions and part labels of piezo-wheat.

piezo-wheat. The actual metric was is shown in Equation (6),

$$Perf = |f_s - f_n|^{-1} \tag{6}$$

where f_s is the frequency of vortex shedding and f_n is the frequency of the device. The damped natural frequency of the device, described in Equations (7), was based on the undamped natural frequency, f_{ud}, an approximation of linear (instead of angular) motion in the device, and a corresponding approximation for the spring constant, k, and mass, m, as well as a calculation of the damping factor, ζ.

$$f_n = f_{ud}\sqrt{1-\zeta^2} \qquad f_{ud} = \sqrt{\frac{k}{m}} \tag{7}$$

The spring constant, k, was obtained by measuring the linear deflection of one of our devices at the midpoint of the stem, and assuming the approximated linear deflection would be the same. The mass, m, was calculated my multiplying the density of plastics assumed to be used for the device and the parts volumes from the geometric model, calculated by a built in MATLAB function convhulln(). The damping factor was calculated using Equation (8),

$$\zeta = \frac{1}{4}\left(\frac{\rho D^2}{m/L}\right)\left(\frac{U}{f_{ud}D}\right)C_d \tag{8}$$

where ρ is the density of air, D is the width of the sail, m/L is mass per unit length of the device, and C_d is the drag coefficient. This model of damping was obtained from Blevins [6], and assumes small amplitude vibrations in high Reynolds number flow, a uniform velocity distribution, constant

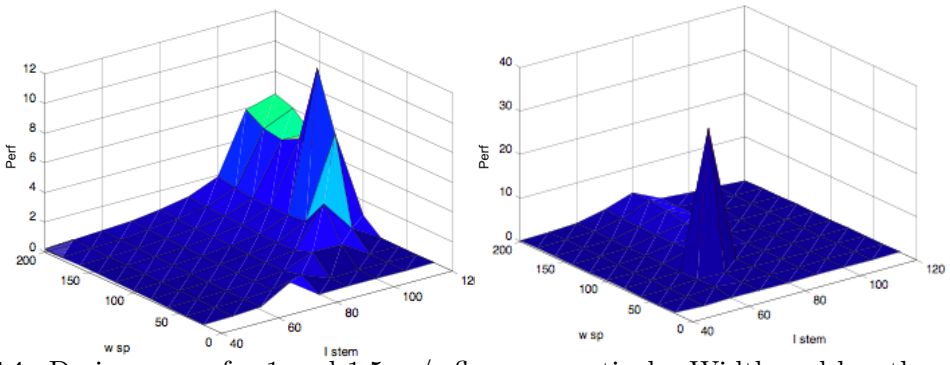

Figure 14: Design space for 1 and 1.5 m/s flow, respectively. Width and length were varied.

drag coefficients, single mode vibration, and motion only perpendicular to the direction of flow. The value of C_d used was 0.8, which was a general assumption for testing, and a model for C_d based on shape would be needed for more accurate results.

The frequency of vortex shedding was calculated as $f_s{=}SU/D$, where S is the Strouhal number, which was assumed to be 0.2 for this model [6]. The expanded equation for the performance metric is shown in Equation (9).

$$Perf = \left| \frac{SU}{D} - \sqrt{\frac{k}{m}(1-\zeta^2)} \right|^{-1} \tag{9}$$

Code for this performance model can be provided by the author on request.

5.3 Design Space Exploration

The beginning stages of optimization were begun in this project by setting up a design space search. Nested loops were created to run a function calculating the performance metric over a broad range of input parameters. An example of the output of the design space exploration is shown in Figures 14.

5.4 Geometric MATLAB Model

A 3D geometric model was created in MATLAB, with all of the parts highly parameterized. The final format of the design parts was the MATLAB patch format. The main physical dimensions of the model, width, depth and length, are shown in the left graphic in Figure 13, and the labels for the individual parts modeled are in the right graphic of Figure 13.

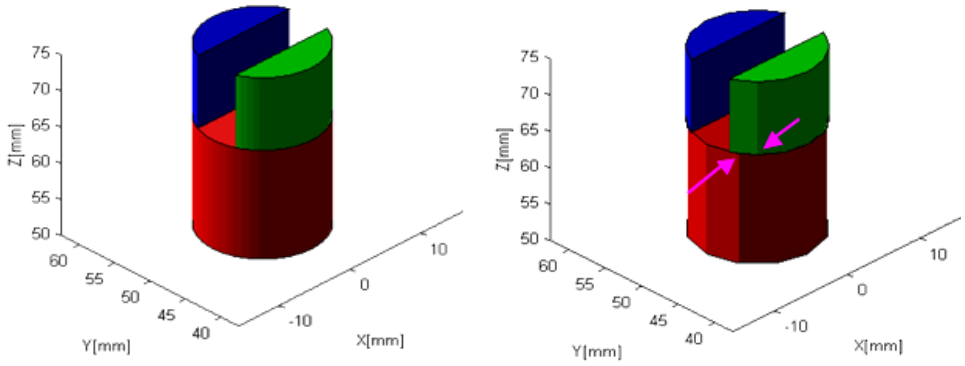

Figure 15: Initial peg model. Higher resolution on the left, and lower resolution, showing discontinuity, on the right.

5.4.1 Methods

The geometric modeling in MATLAB was originally intended to build solely on functions created for previous ME6104 homework assignments, but problems quickly arose. The piezo buzzer was modeled without much trouble using functions similar to that used to create an airplane fuselage in a homework assignment for ME6104. And because the buzzer would be purchased and never need to be fabricated from an STL, this was sufficient. Problems came up, however, when modeling the peg. Initially, the peg was modeled as a cylinder and two separate extruded arcs, as shown in Figure 15, where the angles of the arcs were set such that the resulting gap would be equal to the total thickness of the buzzer.

When rendered at higher resolution (i.e., with more control points) the part looks to be continuous, but a lower resolution part, shown on the right in Figure 15, clearly shows that the vertices of the cylinder and arc extrusion (marked with pink arrows) do not match up. Continuity would have been hard to achieve for any buzzer thickness, so a new approach was taken for modeling the parts.

A freely available MATLAB function, patch2stl, was found on the online MATLAB File Exchange that could convert MATLAB surface patches to STL file format. The MATLAB patch format was investigated, and it was decided that this would be a very adequate method for modeling the parts for this project. The main components of a patch are an $n \times 3$ array of vertices, where n is the number of vertices each column corresponds to x, y and z position, respectively,

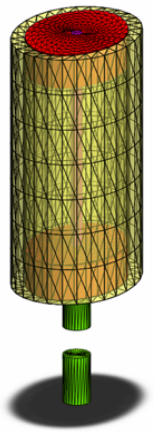

Figure 16: STL file output, ready for rapid prototyping, viewed in SolidWorks.

and a face array which references the row index of vertices and groups them into faces. The order of vertex reference for each face, using the right hand rule, determines the outside normal vector of the face. Many faces could be created as surfaces using Bezier functions from the homeworks or built in functions such as cylinder(), which could then be converted using surf2patch() with the triangles option (to create triangular faces, which is required for STL files) but many features had to be created differently, and conversion to patch format had to be performed manually. This added an extra level of difficulty, as the large number of faces on the parts required numerous loops to assign the vertices to them, and all assignment scripts had to be able to accept a broad range of varying dimensions and resolutions. Details of the methods for the geometric model are provided in Appendix A.

5.5 Results & Conclusions

The 3D geometric model was completed in MATLAB, which allowed full visualization of all parts, exporting most of them as STL files, and a model was created to evaluate performance, which was used to explore the design space. Example of the 3D model parameterization is shown in a comparison of Figures 1, 2 and 10. An example of the result of the conversion to STL files is shown below in Figure 16.

The metric for performance will need to be changed, as the matching of frequencies is not a direct measure of power output. Also, it might prevent design convergence as different frequencies could be converged on. This is demonstrated in Figure 17, which shows the top ranking design

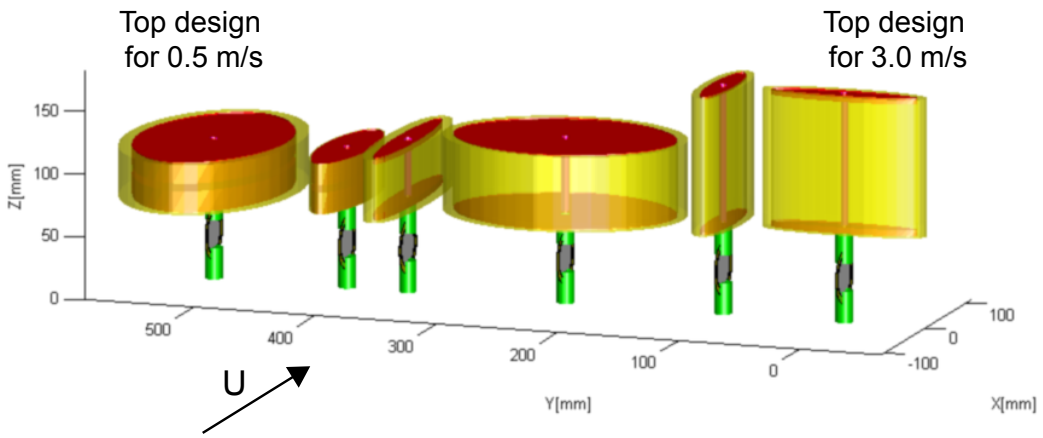

Figure 17: Top designs for 0.5-3 m/s, left to right. Direction of wind is shown by U. When the model was tested at 0.5 m/s, the design on the far left was the best, at 1.0 m/s, the second from the left, etc. Several designs were at edge of design space.

from explorations at different wind speeds.

Future work would require validation and a more defined performance metric. Once this had been done, the model could be tested with simulated wind speeds following a probability distribution that fit an area where the devices could be installed. Also, the model could be modified to incorporate wake interactions from multiple devices. Multiple devices arranged in specific configurations can be key to increasing power output, as was explored later in this thesis research.

CHAPTER VI

MULTIPLE DEVICES: FLOW VISUALIZATION

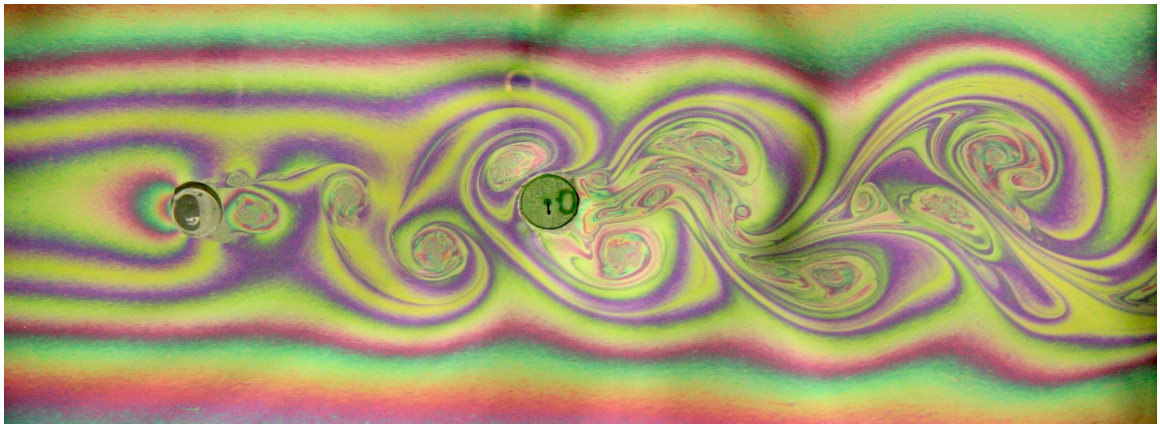

Figure 18: Soap film flow visualization. Sample color image of flow, left to right, around two disks. Vortices shed by the first disk influence the oscillation of the second disk. For reference, the disks are 1 cm in diameter.

In this chapter we present a flow visualization setup with a disk system that is a dimensionally matched approximation of our energy harvesting system. We begin testing rows of devices, as wind tunnel tests, presented in Chapter 7 were beginning to find that downstream devices harvested more energy than upstream devices. Our apparatus is described in depth in Section 6.2, for those interested in recreating our setup, and our new method for measuring film velocity is presented in the same section. We also describe how the systems are dimensionally matched, and we present results from testing the soap film system.

6.1 Background

Soap films are a relatively new method for flow visualization in fluids, with some of the first work being done by Couder in the mid-1980's. A summary of the history of soap films for fluid dynamics research is presented in Section 3.3. The methods used here most closely resemble those presented by Rutgers [45], where a continuously flowing vertical film is utilized to provide flow visualization. Flow patterns are embodied as variations in thickness in the soap film as it flows around bodies inserted into the film. These thickness variations are illuminated via constructive and destructive

interference of monochromatic (seen in Figures 38 and 21) or white (seen in Figure 18) light reflected off of the film, which is then captured using video or still cameras. These light patterns have been shown to closely match streamlines [59, 45] and are a good approximation of two dimensional flow [7, 28].

6.2 Soap Film Apparatus

A diagram explaining our soap film apparatus is shown in Figure 19. The height of the entire stand was approximately 2.1 m, allowing for test specimens to be inserted into the film approximately 60 cm from the nozzle. This distance allowed for the film to be flowing at near terminal velocity [44, 59], where the flow velocity was controlled by the flow rate through the nozzle and limited by drag against the air. A set of wires were used to spread the main wires, once the flow had started, to a width of approximately 10 cm. The spreading wires were connected to a metal clip, and their lengths were adjusted such that simply pulling the clips up and inserting them into holes cut in the side of the soap film frame would hold the main wires at the proper width. A weight at the bottom provided tension on the main wires.

A diagram detailing the top portion of the apparatus is shown in the right side of Figure 19. Flow control and measurement was provided by a precision variable-area rotameter capable of measuring 5 – 52 ml/min of water, OMEGA Engineering part number FL-3665G, which included a built in multi-turn valve. The inlet of the rotameter was connected via a hose to a large reservoir above it, capable of holding 5 liters of solution. The area of this reservoir was large, such that 5 liters of solution was only about 5 cm deep. This insured that variations in the pressure head in the system would be negligible though the duration of a test. The hose used for this connection included a built in self sealing quick-release, allowing for easy removal of the reservoir for solution replacement.

The outlet of the rotameter valve was connected via a hose to a pipet nozzle, which was suspended in the center of the top of the soap film stand from a brass t-joint. This end of the pipet nozzle was trimmed, such that the opening was about 1.5 mm wide. The pipet nozzle was attached to the hose by trimming the other end of it until it could be press fit into the flexible hose, and sealed with plumbing tape. The main wire used for the soap film was 20 pound test nylon fishing

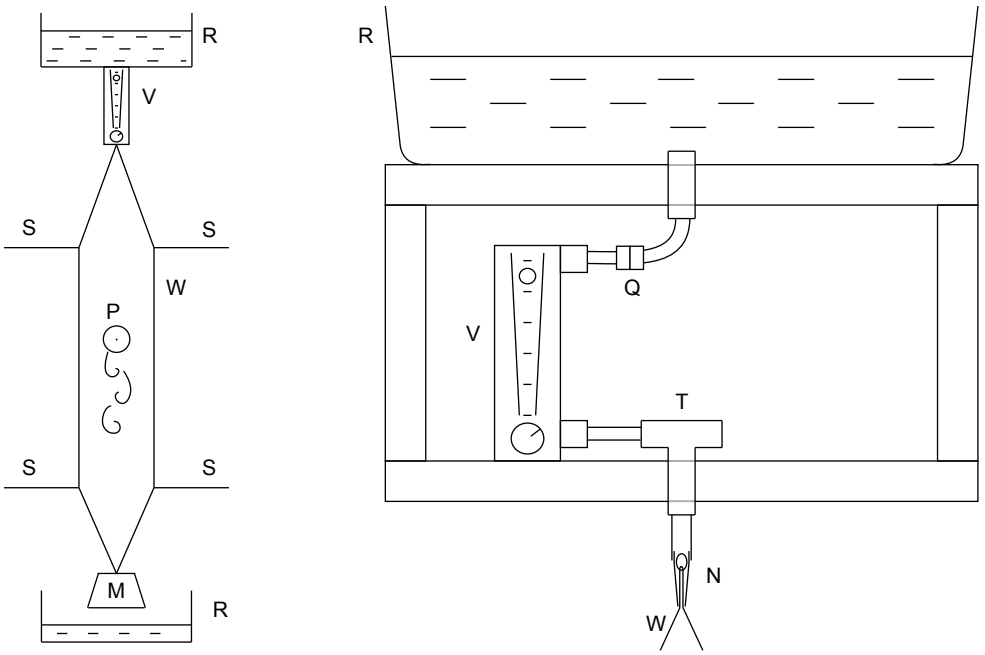

Figure 19: Soap film tunnel layout. The left diagram details the entire apparatus, and the right diagram is a detailed view of the top portion of the apparatus. Features include reservoirs (R), rotameter/valve (V), main wires (W), side wires (S), tension mass (M), quick-release and hoses (Q), T-joint (T), and nozzle assembly with metal loop holding main wires (N).

line, which was tied at the bottom of the stand to a weight, and looped into the pipet nozzle, around a small metal wire ring which fit in the top of the nozzle, but could not fit through it, and then back out the nozzle. This allowed for film to form smoothly at the opening of the pipet, without requiring the nylon wire to be pulled through the valve.

Test specimens around which flow was tested were held in the film by metal wires and a system of clamps, as demonstrated in Figure 20. A 55 watt low pressure sodium lamp was the monochromatic light source [59], with a custom built fixture that used a parabolic reflector and a frosted acrylic cover to provide the most even lighting possible. Flow patterns were captured using a Canon 50D DSRL with a 50mm f/1.8 lens for still images and a Vision Research Phantom V9.1 high-speed camera with a 50mm f/0.95 lens for still images and high speed video. An example of the visualization that could be obtained is shown in Figure 21.

6.2.1 Velocity Measurement

As the velocity of the soap film was highly variable, a reliable method was needed to measure the velocity of the film. High-speed video was used to estimate flow velocity by tracking the distance particles and disturbances in the film traveled over a given number of exposures, but

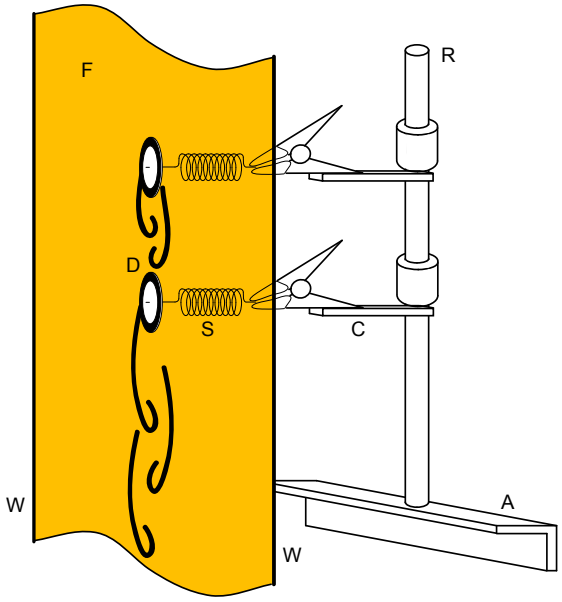

Figure 20: Diagram showing disks (D) suspended from springs (S) in the soap film (F). The clamps are vertically adjustable along a rod (R), which is fixed to an angled aluminum support (A). The wires (W) that support the film are also shown.

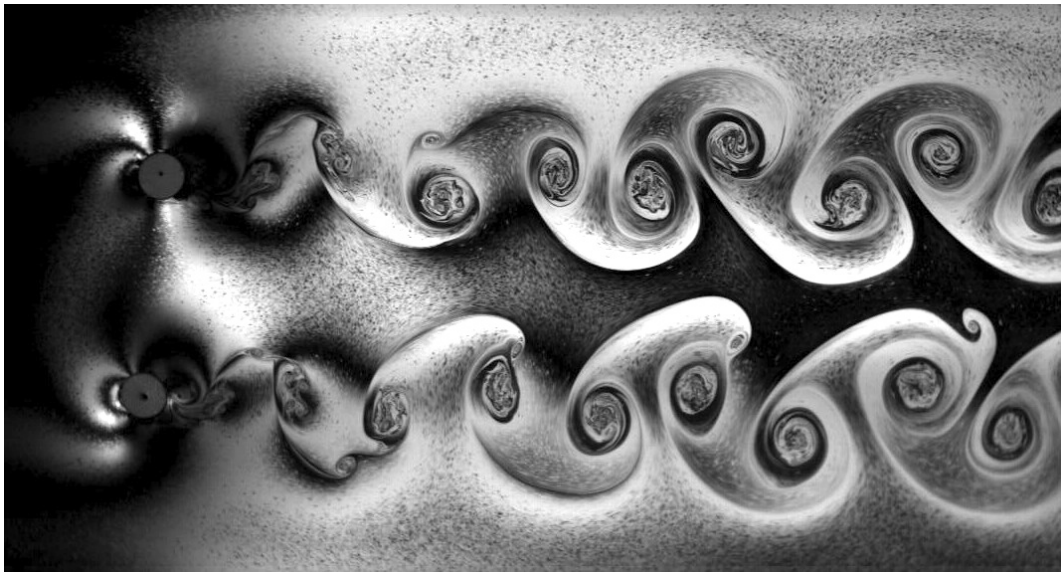

Figure 21: Example of soap film visualization, with two disks side-by-side. Flow is from left to right.

this method could only provide velocity readings long after an experiment was carried out. Other existing methods included using laser doppler velocimetry, a hot wire anemometer, optical fiber velocimetry [22, 42] and particle image velocimetry (PIV) [44]. Each of these possible solutions were ruled out, either due to excessive cost, complexity, or lack of real-time velocity data.

As extreme accuracy was not required for the purposes of our flow visualization, a new method was developed for estimating flow velocity. Film thickness has been shown to be primarily a function of a surfactant concentration [4], and to a lesser degree, flow rate [4, 44]. As film width and solution concentration could easily be controlled, a correlation was found experimentally between the measured flow rate through the rotameter and the velocity of the film, 60 cm down from the nozzle. This one time calibration using high-speed video to measure film could then be used to estimate flow velocity by reading the flow rate from the rotameter and then finding the corresponding velocity on a calibration curve. An example of two different exposures used to calculate velocity is shown in Figure 22, where unique patterns and small imperfections in the film were tracked over a known period of time. The distance traveled by these features could then be measured in pixels, and converted to millimeters using a ratio taken from reference image with a ruler in the plane of the film.

The resulting calibration curve is shown in Figure 23. Data from five different tests is shown, and it can be seen that the maximum error observed was below $\sim$5%. The non-linear nature of the curve is most likely explained by the dependence of film thickness on its velocity.

6.2.2 Dynamically Matched System

Once flow visualization had been provided by the soap film, with a velocity that could be controlled within the required accuracy and precision, a matched system to compare with the 3D piezoelectric cylinder system was developed. Testing started with a single fixed cylinder, with which vortex shedding could be observed, and the Strouhal number could be measured using Equation (10).

$$S = \frac{f_s D}{U} \tag{10}$$

A styrofoam disk was used with a diameter of $D = 12.5$ mm, flow velocity ranged from $U = 1$ to 1.5 m/s, and the frequency of vortex shedding, f_s, was measured at 18 to 22 Hz, respectively. Vortex shedding frequency was measured where a single period includes a full left-right vortex pair

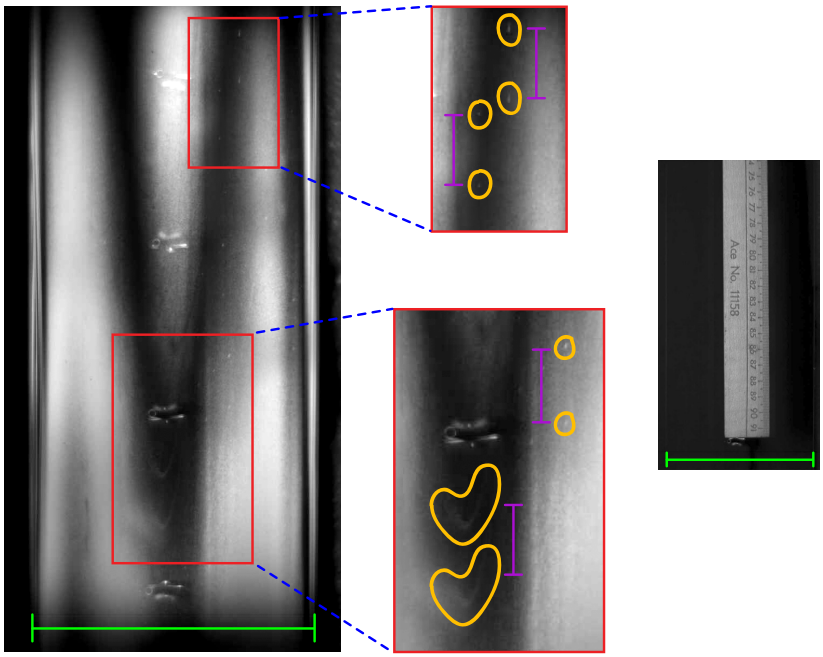

Figure 22: Example of video frames used for flow meter calibration. Two frames, taken 10 ms apart, have been merged. Two sample areas, highlighted in red, show unique disturbances (yellow) in the flow that have traveled a certain distance (purple) between the two exposures. This distance was measured in pixels, then converted to millimeters using the reference image on the far right, where the distance between the nylon wires is marked in green for scale.

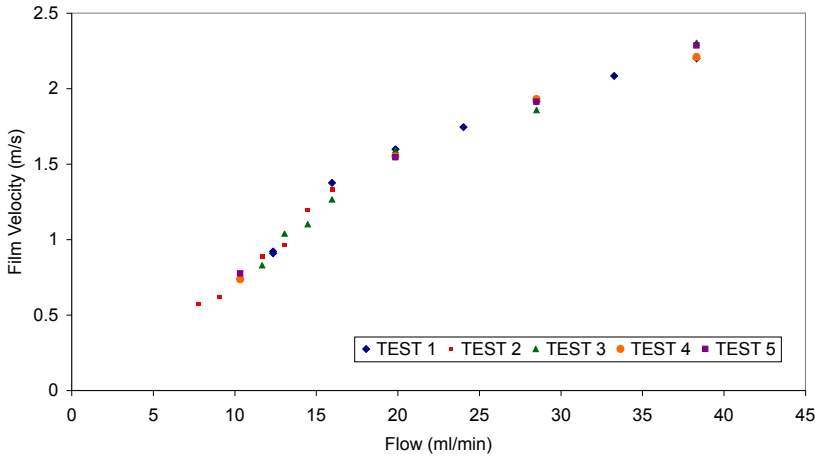

Figure 23: Flow rate to velocity calibration. Velocity was measured over a range of flow rates, over several different tests. Flow rate was calculated from flow meter readings using manufacturer provided data.

[6]. The resulting calculated Strouhal number, S, was between 0.19 and 0.21 for the tests. This matched very closely with the expected 0.21 [15], obtained from Equation (11).

$$S = .212\left(1 - \frac{12.7}{Re}\right) \tag{11}$$

For these tests, the Reynolds number, Re, ranged from about 3000 to 4500. These values were obtained using Equation 12,

$$Re = \frac{\rho U D}{\mu} \tag{12}$$

where the density of the soap film, ρ, was essentially that of water at room temperature, 998.2 kg/m^2, V was the velocity of the film, and μ was the viscosity of the film, which was estimated to be 0.00399 kg/m-s from similar work done by Zhang, et at. [59].

The first attempt at matching the wind tunnel system was done with four disks in line, with as many parameters as possible matched to the 3D system. These parameters, all dimensionless groups, included the spacing ratio, L/D, Reynolds number, frequency ratio, f_s/f_n, and mass ratio, m^*, where the last two parameters are defined in Equations (13).

$$\frac{f_s}{f_n} = \frac{SU}{\sqrt{E/\rho_c}}\left(\frac{H_c}{D}\right)^2 \qquad m^* = \frac{\rho_c H_c}{\rho_f H_f} \tag{13}$$

Here, ρ_f and H_f are the density and height of the fluid, and ρ_c and H_c are similar values for the cylinder, and E is the effective modulus of elasticity of the cylinder. To match the 3D system as closely as possible, styrofoam disks with diameter $D = 12.7$ mm and hight $H_c = 1.5$ mm were used. The material had a density of $\rho_c \simeq 75$ kg/m^3. To make the disks elastic, each was mounted on a spring, as shown in Figure 20. This resulted in a damped natural frequency of $f_n = 22$ Hz, measured experimentally, while inserted in the film. The Strouhal number was assumed to be constant at $S = 2.0$. The density of the soap film was assumed to be that of water, $\rho_f = 998.2$ kg/m^3, and the height of the film (thickness) was assumed to be $H_f = 3$ μm [59]. These parameters resulted in a mass ratio of $m^* = 32.6$ and a frequency ratios of $f_s/f_n = 0.8$ – 2.0 for flow rates of 1.1 – 2.8 m/s, respectively. These values can be compared to the same parameters for the 3D system, as is shown in Table 2. For equivalent frequency ratios, the Reynolds numbers are within approximately 10% of each other, which was considered a very good match. There is about a 3$\times$ difference in the mass ratios, but it was decided that a difference of less than one order of magnitude was sufficient.

Table 2: Comparison of key parameters between 2D soap film system and 3D wind tunnel system.

Parameter	2D System	3D System
f_s/f_n	0.8 – 2.0	0.8 – 2.0
U (m/s)	1.1 – 2.8	1.8 – 4.3
Re	3550 – 8900	4100 – 9800
m^*	30	80

6.3 Methods

Using this new setup, four disks were suspended from springs and placed in tandem in the soap film. These first tests were performed before the rotameter was added to the system to precisely control flow speed, and instead, a simple valve was used to adjust flow rate. It was believed that the valve handle could be manually set to the same angle for each repetition of the test, and that the resulting flow speeds would be close enough for satisfactory repeatability. The first test was to vary the spacing from L/D from 4.5 to 7, and to see if the trends in mean velocity of oscillation were similar to data collected in the wind tunnel with piezo devices.

Two tests were run at each spacing to insure variations in flow speeds were not significant, and each test was filmed for 5 seconds with a high speed camera. The need for a test duration of at least 5 seconds is demonstrated in Figure 24. Here, the position of each of 4 disks, measured in image pixels, is shown for 1 second. It can be seen that, while the motion is very periodic, there are fluctuations in amplitude over time. The resulting frames from these tests were processed with a series of MATLAB functions and scripts. The first script was used to account for variation in brightness of the image due to the 60 Hz flicker of the lamp. This was done by selecting a reference area in a fully lit image, and calculating the average brightness of the pixels in that area. Then the brightness of each image was scaled such that the reference area would have the same brightness. Then, a function would go through all of the frames, recording the X and Y coordinates, in pixels, of white dots placed on the center of each disk. A series of filters were implemented here to only find portions of each image that were the right size and shape, as there was significant noise due to the constantly changing flow patterns also present in the video. Over the course of this project, this particular function was modified extensively, optimizing it for efficiency and accuracy. The MATLAB code for this function is given in Appendix B.1. From the positions of each disk over

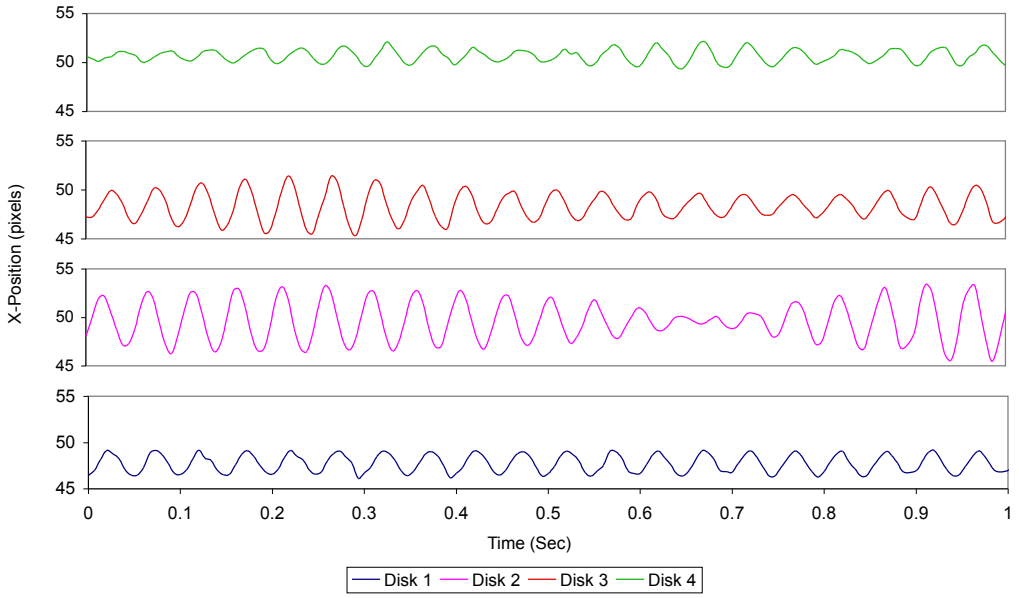

Figure 24: Position of 4 disks in soap film over 1 second. Significant variations in amplitude over the 1 second test can be seen, especially in disks 2 and 3.

time, the velocity over time was then calculated, with a filter to remove outlying position data due to occasional errors. As described in Chapter VI, the average power output from our piezo devices is linearly proportional to the average velocity at which it oscillates (Equations (5) & (4)). The velocity of the disks in the film and the voltage output of the piezos in the wind tunnel could therefore be used to compare trends between the 2D system and 3D system.

6.4 Results

Results of these experiments are shown in Figure 25. The wind tunnel data clearly shows that for all spacings tested, there is a trend for voltage to increase from the first to third devices in the row, and then to decrease slightly for the fourth. This trend is shown in some of the soap film data, but there are significant variations, and even more important, the soap film data was not repeatable for most tests. For example, in Figure 25, the two soap film tests at $L/D = 3.3$ (blue circles and triangles) are very similar to each other, but they are very different from the trend seen in the wind tunnel tests (blue squares). At spacing $L/D = 5.4$, one of the soap film tests closely matches the wind tunnel test (red triangles and squares), but is very different from the second soap film test (red circles). It was determined that the largest contribution to these variations between two of

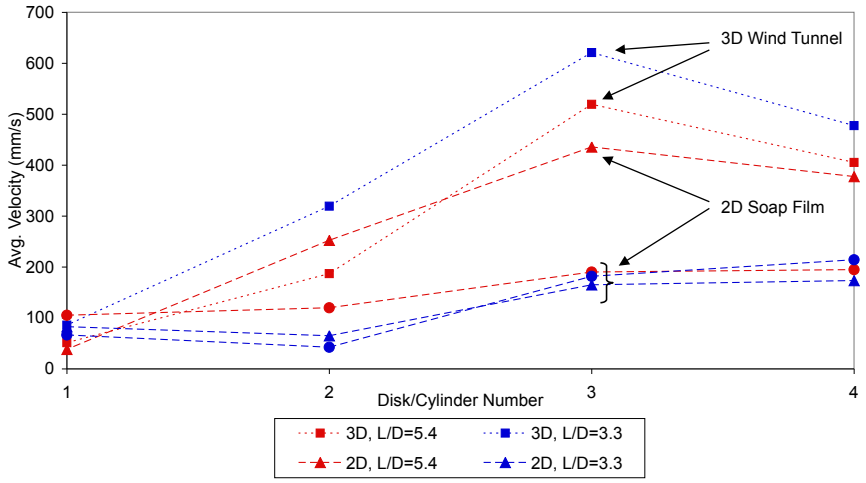

Figure 25: Comparison of trends in 3D and 2D systems with four cylinders/disks. Output from both systems is reported in average velocity, which is linearly proportional to power for the wind tunnel system. Spacings of $L/D = 5.4$ are shown in red, $L/D = 3.3$ in blue. The 3D system is marked with squares and the 2D tests are marked in circles and triangles.

the same tests in the soap film was irregularity in the film velocity. Manually measuring the flow velocity from each test, using the methods shown in Figure 22, revealed after testing was completed that there were significant variations in film velocity, several times in excess of 50%.

After the new apparatus with the rotameter was assembled and calibrated, testing resumed in the 2D soap film system. As a starting point, it was decided that a simplified system with only two cylinders, the first fixed and the second suspended from a spring, would be used for testing. This was done to eliminate some of the variability in results, as the physical setup was very sensitive to slight changes, and it would reduce the data to be focused on to a single output instead of four. Faced with the design variables of spacing and frequency ratio, it was determined that frequency ratio would first be investigated before expanding testing into ranges of both design variables. A series of tests were performed at a fixed spacing of $L/D = 6$, with the frequency ratio ranging from $f_s/f_n \simeq 0.7 - 1.2$. A total of 18 tests were performed, two each at 9 different frequency ratios. The results of these tests are shown in Figure 26, where the data labeled "A" are from the first set of tests, and "B" are from the second.

To better understand the data, sample flow patterns from each test were compared, and disk velocity data was analyzed in the frequency domain using discrete fast Fourier transforms (FFTs).

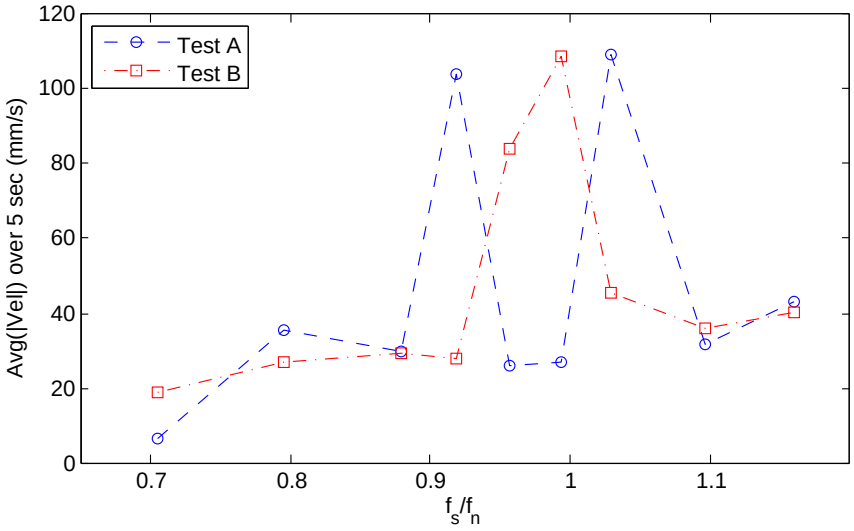

Figure 26: Results from an oscillating disk behind a fixed disk, with spacing $L/D = 6$, in a soap film as frequency ratio is varied. Average of absolute velocity, which would linearly correlate to power from piezos in the 3D system, is measured. Each value of f_s/f_n was tested twice, resulting in Tests A and B.

A sample FFT is shown in Figure 27, and flow visualization is shown in Figures 28 – 31. Correlations could clearly be seen between the FFTs and the data in Figure 26. For example, Test B is significantly higher in Figure 26 at $f_s/f_n = 0.95$, and the FFT of Test B is much higher in Figure 27.

The images of flow patterns in Figures 28 – 31 also have correlations that can similarly be drawn with the data in Figure 26. In general, the vortices behind the second disk are more fully developed, and have a wider wake, for the tests with the higher outputs. While the images in these figures are only single frames of 1000 captured for each test, they were selected as being representative to the entire test. These more fully developed vortices could be due to the second cylinder being locked in phase with the vortex shedding from the first cylinder, and the images corresponding to lower output could show less developed vortices due to the second cylinder being slightly out of phase. This could indicate that the system has multiple stable states, or, at the very least, indicates that it is not perfectly stable.

The significant inconsistency between the two sets of tests around resonance was not expected, or fully understood. It was believed that either the system was simply very sensitive to small changes, and, for example, the disk may have moved on the spring, changing f_n, or more likely,

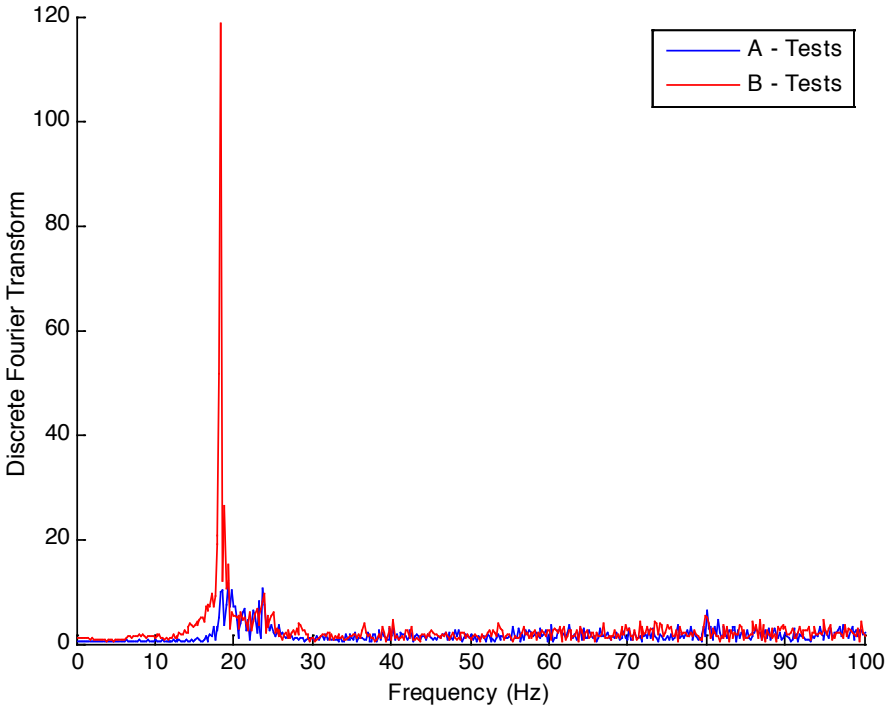

Figure 27: FFT for $f_s/f_n = 0.95$. Note that the significantly higher amplitude of Test B around 20 Hz agrees with the output of Test B at $f_s/f_n = 0.95$ in Figure 26.

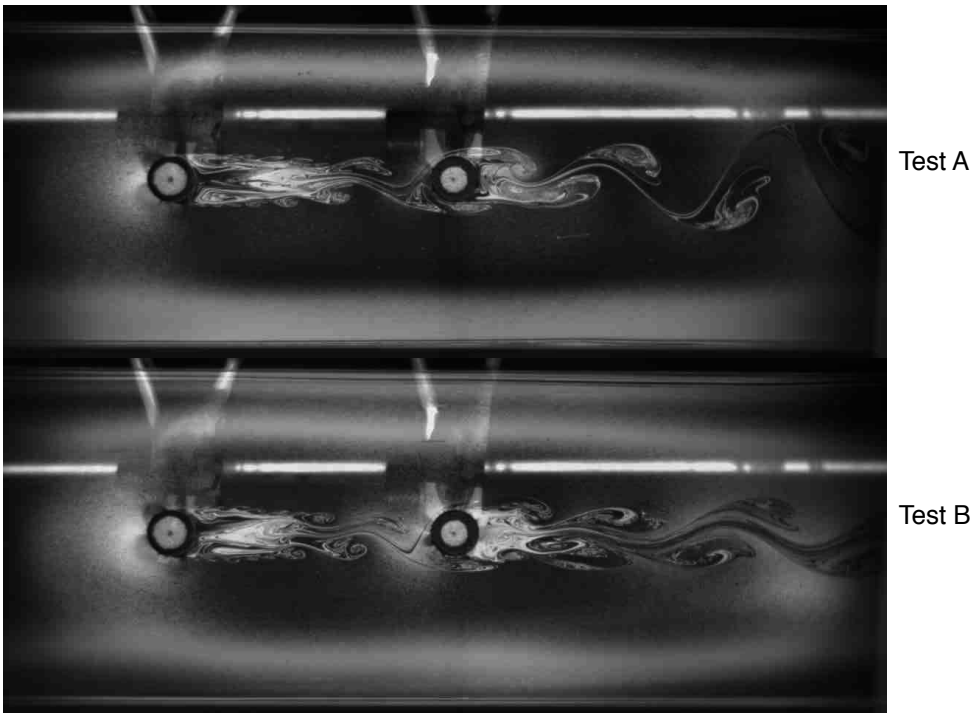

Figure 28: Flow patterns for $f_s/f_n = 0.92$. Note that Figure 26 shows a significantly higher output for Test A, and the vortices behind the second disk in Test A are larger than in Test B.

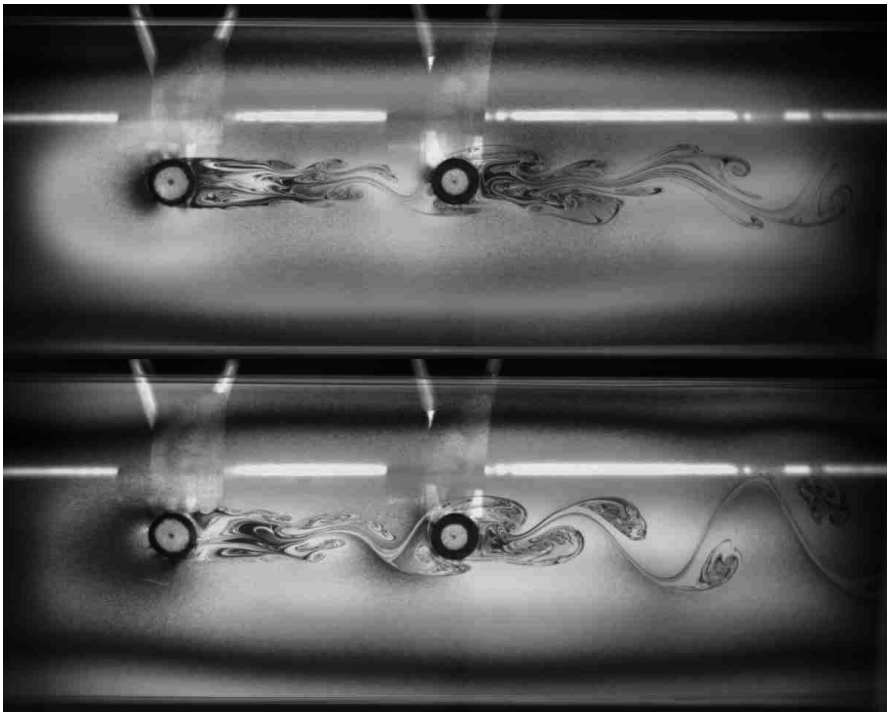

Figure 29: Flow patterns for $f_s/f_n = 0.95$. Note that Figure 26 shows a higher output for Test B, and that the vortices behind the second disk in Test B appear more developed and have a wider wake than in Test A.

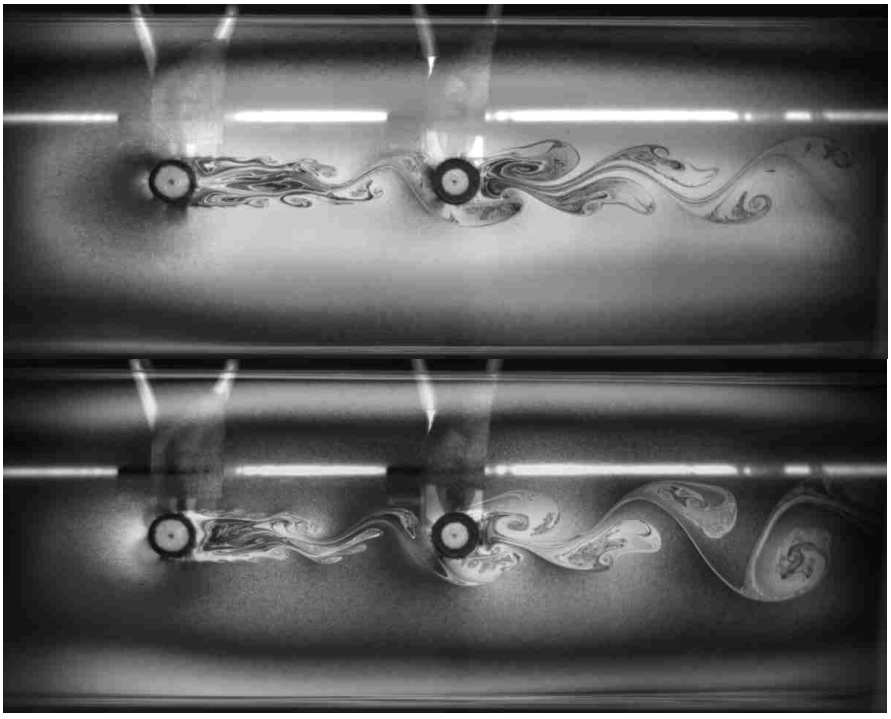

Figure 30: Flow patterns for $f_s/f_n = 1.0$. Note that Figure 26 shows a significantly higher output for Test B, and that the vortices in Test B appear larger than in Test A.

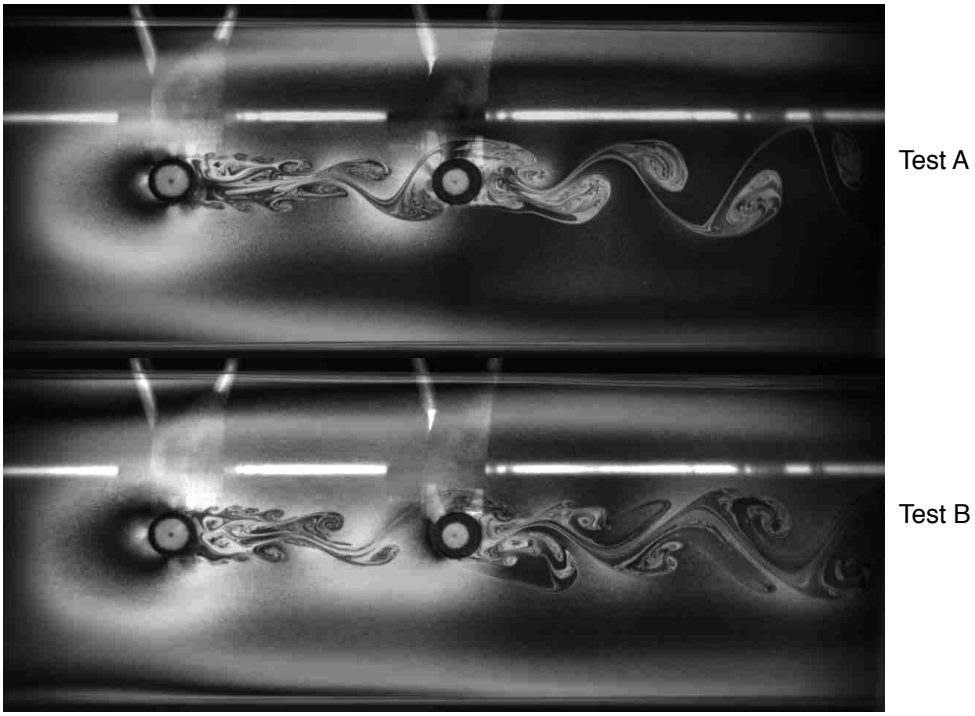

Figure 31: Flow patterns for $f_s/f_n = 1.10$. Note that Figure 26 shows a very little difference from the output of Tests A and B.

the system could have had multiple stable states. Tests were repeated near resonance a total of twelve more times, where four of those tests involved gently flicking the cylinder 30 seconds prior to data collection. This would start the cylinder oscillating, while the damping of the system and the 30 second interval insured that the disk was at steady state before the test began. This was done to test the theory of multistablity — if the power output was higher for these tests, it could be possible that the system was multistable, and the flick would force it into the state of higher amplitude oscillations. The results from these test, along with the previous data, are shown in Figure 32.

6.5 Conclusion

With three of the four "flick" tests resulting in higher than average output, it is believed that the the system is likely to be multistable, although further testing would be required. This testing also indicated that, stable or not, it might be possible to get repeatable results on average with large numbers of tests. The problem with this approach was that the process of data collection was very time consuming, due to several factors. The soap film was relatively difficult to work with when

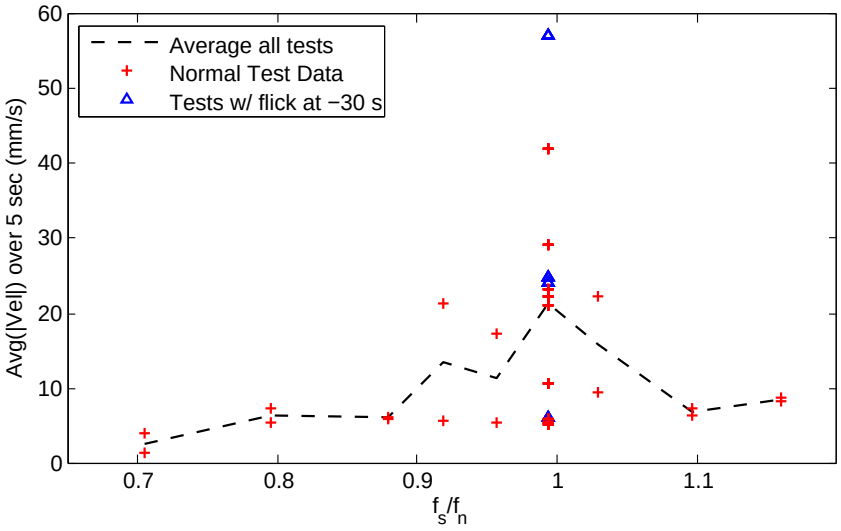

Figure 32: Results from an oscillating disk behind a fixed disk in a soap film as frequency ratio is varied, with extra tests at resonance. Similar to Figure 26, but with 12 more tests at resonance. Blue triangles mark results from tests where the disk was manually oscillated 30 seconds prior to the start of the test to determine if the system was bistable.

multiple objects had to be inserted into the flow. The robustness of the film was very low, making it very easy to burst by accident. Also, it was very sensitive to build up on the lines, and the solution would have to be replaced often, but would need to sit for up to a day after being mixed. Once tests were run, the collection of data from the video was relatively slow as well. Processing 1000 frames for a single test took at the very least 10 minutes, and time had to be spent in the middle of the process to insure that the image brightness correction was done properly, and that other settings such as the grey threshold level were set properly.

While the soap film provided valuable flow visualization, and showed promise for a matched 2D system, obtaining data was significantly more time consuming than in the wind tunnel system. We decided that a broader range of tests should be conducted in the 3D wind tunnel system using the piezo devices before such time was spent getting more detailed flow data from the soap film system.

CHAPTER VII

MULTIPLE DEVICES: SPACING & FLOW VELOCITY EXPERIMENTATION

In previous chapters, we focused on the behavior of single devices. The goal of this portion of our research was to develop and study a group of devices that could harvest energy from gusts and other unsteady wind motion. This resulted in our latest solution, a crude series of devices that resembles a row of miniature trees that sway in the wind, which harvests energy through the deformation of piezoelectric transducers at the base of the devices. The general layout and function of a single device is shown in Figure 33. The design decision to only allow motion transverse to the flow was based on our early tests. We found that two degrees of freedom would result in dominant motion only in the transverse direction, which, for the mass ratio of our system, agreed with results from Jauvtis and Williamson [21]. There are advantages of this oscillating design over other energy harvesting applications [36, 38, 37, 46, 5]. First is a lack of rotating parts such as gearboxes, which are the most frequently repaired parts of wind turbines. Increased power output when multiple devices are grouped together is another advantage.

This paper focuses on experimentation and results regarding the effects of variations in spacing between devices, and the ratio of vortex shedding frequency [6] to the natural frequency of the devices, on power output. Of specific interest will be the influence of spacing and velocity on flow attachment and structure (see Figure 33), [20, 19]. A critical spacing was found by Zdravkovich and Pridden [57] of $L/D = 3$, which was close to a point of interest for our experiments of 3.3. One approach to increasing the power output could have focused on increasing amplitude of oscillation by optimizing the reduced damping, S_G, as shown in so called "Griffin plots" [23], but layout and flow speed was chosen instead as it was deemed a more interesting problem.

The mechanism by which the devices move and collect energy is referred to as vortex induced vibration [50, 3, 6, 14, 60, 56], where lateral pressure asymmetries caused by periodic shedding of vortices from an individual cylinder (Figure 33) cause it to oscillate, which can also be influenced

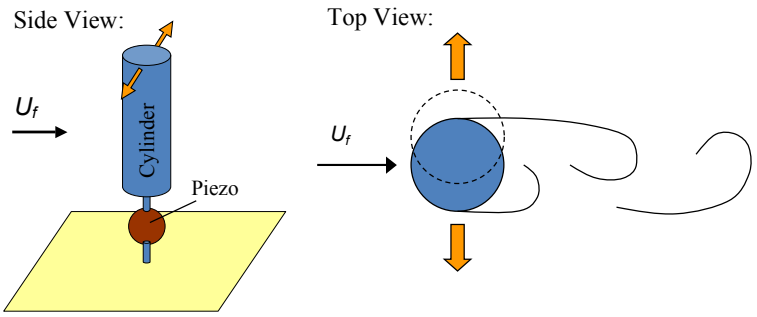

Figure 33: Side and top view of single energy harvesting piezo device. The speed of the incoming fluid is U_f. Instantaneous streamlines are included to demonstrate vortex shedding in the top view.

by vortices and other flow structures from a single upstream cyclinder [29, 30, 2, 25, 31] or multiple upstream cylinders [24, 51]. The work of Igarashi was with fixed cylinders, and Lam and Tatsuno was with cylinders in different triangular arrangements. What seems to be lacking, however, is work with larger numbers (>2) of oscillating cylinders all in tandem.

7.1 Methods

For all experiments, the voltage from each piezo was individually measured across a 1 MΩ resistance, at a sampling rate of 200 Hz using a PC with a multichannel data acquisition board running LabView^{TM}. The power output, P, for each device was then calculated from voltage resistance, R, using Equation (4).

$$P = \frac{V^2}{R} \tag{4}$$

Root mean square power, P_{rms}, and then non-dimensionalized power, P', were calculated using Equations (14), where P_1 to P_n are individual power measurements, and n is the total number of measurements in a test.

$$P_{rms} = \sqrt{\frac{P_1^2 + P_2^2 + \cdots + P_n^2}{n}} \qquad P' = \frac{P_{rms}}{\rho U^3 D H_c} \tag{14}$$

The cylinder walls were made of 35 mm inner diameter, 0.4 mm thick polyethylene storage tubes, cut to a length of $H = 78$ mm. These were attached to a 4.7 mm diameter, 22 cm long bamboo rod with two styrofoam spacers. A slit was cut in the base of the rod, ∼1 cm deep, and it was epoxied to the piezoelectric transducer. The piezos were manufactured by PUI Audio, part number AB4113B, and intended for use as audio buzzers. They were double layer ceramic piezos,

with a 42 mm diameter brass plate between the layers. On the base of the piezo, a peg was epoxied on, similarly to the bamboo rod, which would fit into a grid of holes on a wooden board, spaced 1.5 inches apart, to allow for different arrangements of devices. The two layers of the piezo were connected in series, and wires were then run from each to a breadboard, from which voltage readings were taken. To tune each of the devices, such that its resonant frequency was 11 Hz, common metal paper clips were attached to the top of the bamboo rods, and slid up an down the rod to change the rotational moment of inertia. A photograph of the four devices on the wooden peg board is shown in Figure 34.

A photograph of the four devices used for out tests is shown in Figure 34. The piezoelectric transducers and cylinders are labeled - also shown is the pegboard base on which the configuration of the devices could be quickly changed, the stems on which the cylinders could be slid to adjust mass distribution, and the wires from which the voltage from the piezos could be measured. Figure 35 demonstrates the full experimental layout, including the four devices, the base, and the square cross-section wind tunnel. Dimensions of the tunnel, as well as the numbering system for the devices relative to the flow direction are noted as well.

Flow velocity in the wind tunnel was controlled by a combination of built-in speed controls on the fan and a 120VAC Variac^{TM} variable transformer. Calibration of the system for flow speed was provided by velocity measurements using a hand held anemometer, insuring that variation in velocity was less than 5% over the area that the piezoelectric devices would be placed.

While the natural frequency of the cylinders was approximately 11 Hz, allowing for sampling over 2 seconds to measure over 20 periods, it was discovered early on that, due to the irregularity of the amplitude of oscillation, longer tests durations were required to get repeatable results. Figure 36 shows a plot of the 60 second moving average of the absolute value of the voltage from each of the four piezo devices during a single test. The high variation in voltage (and similarly, as discussed earlier, amplitude of oscillation) can be clearly seen in the first 5-10 seconds of the data. After 20 seconds, each of the individual data sets seem to converge to their own average values, but even approaching 60 seconds, each moving average has not exactly leveled out. For this reason, tests were carried out with a sampling duration of 60 seconds, and each tests was then repeated 5 times to help insure the reliability of the data.

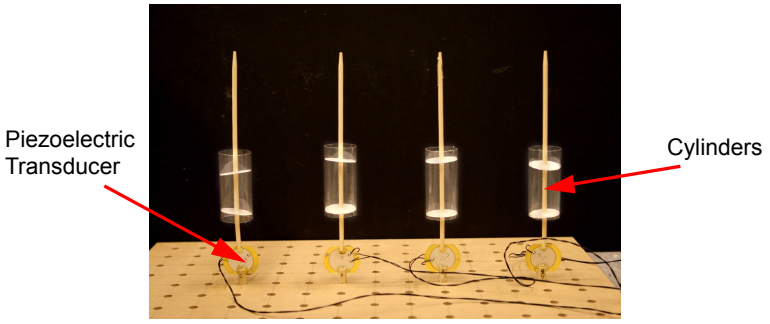

Figure 34: Photograph of four piezo devices in series, with cylinders and piezoelectric transducers labeled.

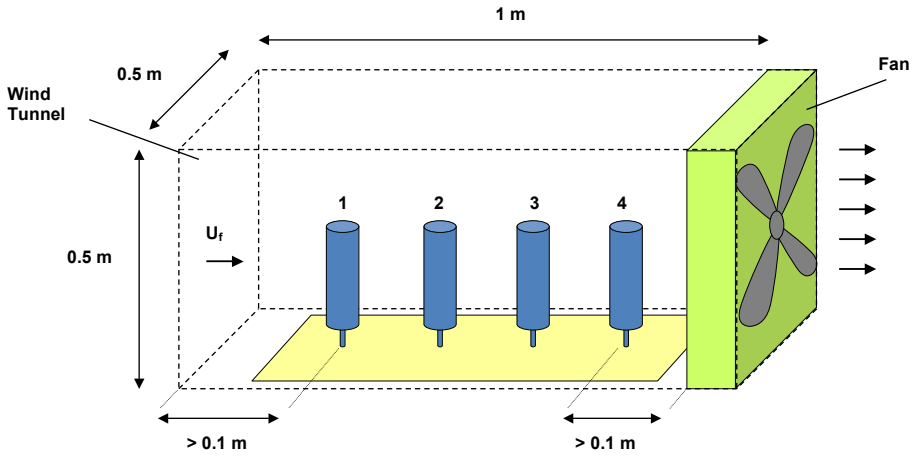

Figure 35: Diagram of wind tunnel layout. Cross section of tunnel is 0.5 m × 0.5 m. Air is drawn through the tunnel, from the left to the right, by the fan on the right. The first and last device in the series were always at least 0.1 m from the ends of the 1 m long tunnel.

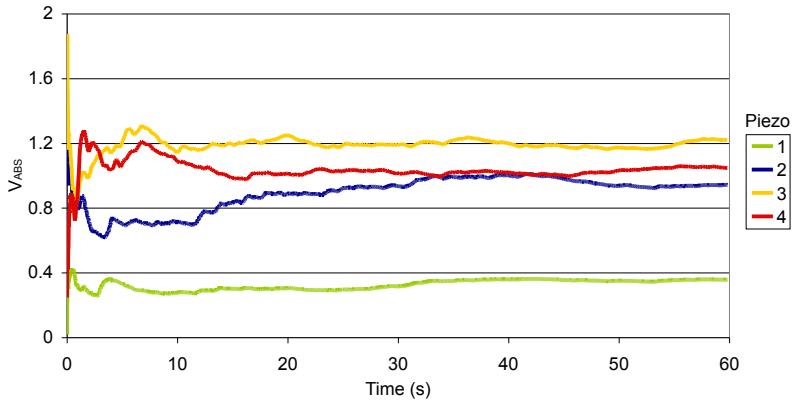

Figure 36: Moving average of voltage output. Absolute value of voltage from each of four devices is plotted to show variation in output over time, and the need for long test periods. Relative output from each device in the row is also shown.

7.2 Results

Experiments were run at six different speeds, and therefore, values of f_s/f_n, and at four different values of L/D, resulting in a design spaceof 24 points, each of which having individual values of P' for each of the four devices. In total, 96 power measurements were taken. This design space is shown in Figure 37, where the values of P' represented by the surface are the cumulative dimensionless power for the four devices. The lowest power was seen at low frequency ratios (0.8 - 1.0) , over which there was little variation as L/D changed. Power increased with frequency ratio, until dropping significantly at $f_s/f_n = 1.8$, and other than at this last frequency ratio, total power was highest at $L/D = 3.3$.

In an attempt to better understand the connection between vortex shedding and power output, a three-cyclinder system was visualized in two dimensions in a flowing soap film [4, 45, 41]. Here, interference patters from light reflected off of a vertically falling soap film were used to approximate streamlines around three cylinders at two different spacings, $L/D = 2$ and 5, and two different flow speeds, which by matching Reynolds numbers, corresponded to frequency ratios of $f_s/f_n = 0.5$ and 1.5. These four combinations of f_s/f_n and L/D are marked on Figure 37 with the letters **A** through **D**, which correspond to images **A** through **D** in Figure 38.

The experimental results can also be visualized without summing the power from each piezo, so that the relative contribution of each device can be seen, by averaging across either all spacings or all frequency ratios. Examples of each are shown in Figures 39 and 40, respectively. The trend of dimensionless power increasing as f_s/f_n increases can be seen in Figure 39, and it can also seen that the relative distribution of power changes at $f_s/f_n = 1.6$. Below this value, the peak power is developed in the third device, while at this point and above, the peak power comes from the fourth device.

Averaging across all frequency ratios, as was done in Figure 40, gives similar results, but with lower values due to the fact that there were larger variations over the span of frequency ratios than over all spacings. Differences in individual piezos are also less apparent, a result of averaging the different power distributions from different frequency ratios. It can also be seen in this representation of the data that the highest power across all frequency ratios is provided at a spacing of $L/D = 3.3$. Figure 41 shows the individual dimensionless power values for the four piezo devices for all

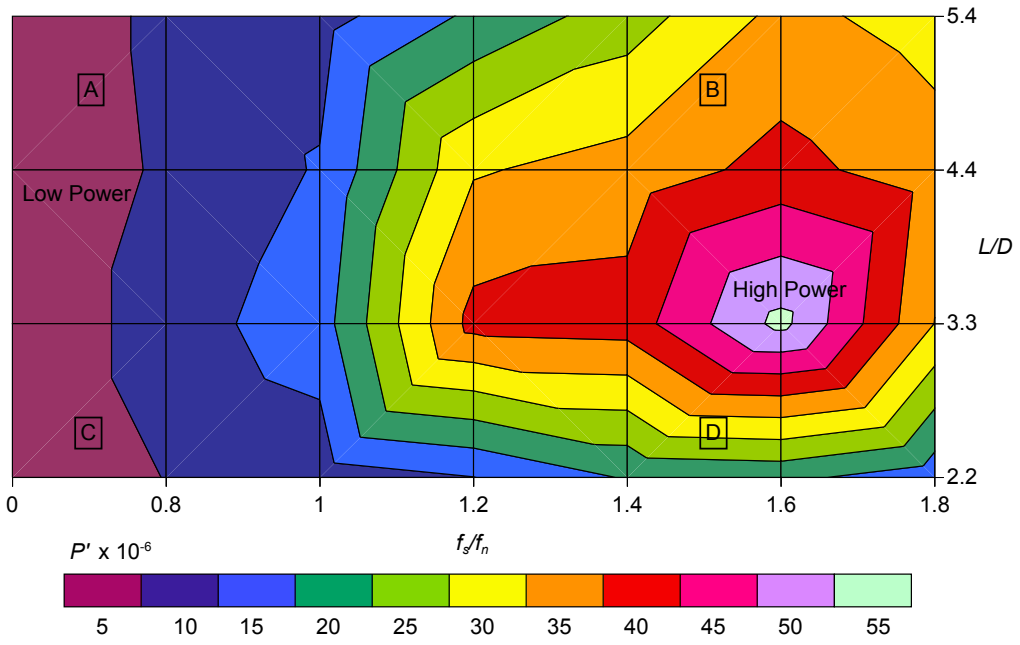

Figure 37: Combined dimensionless power, P', for all four devices as f_s/f_n and L/D are varied. General regions of low and high power are labeled, as are the positions of four specific conditions, **A** through **D**, for which flow around three cylinders was modeled in a soap film (See Figure 38).

frequency ratios, for a fixed spacing of $L/D = 3.3$. The trends are very similar to those in Figure 39, including the transition from the third to the fourth piezo producing the most power at $f_s/f_n = 1.6$, except that the power values are higher, due to $L/D = 3.3$ producing the most power.

7.3 Discussion

Key points of interest are the peak dimensionless power along the line of $f_s/f_n = 1.6$, as well as along at the spacing of $L/D = 3.3$. From work by Zdravkovich [57], it was expected that spacings below $L/D = 3$ would have low power outputs due to a lack of vortex shedding behind the leading cylinders, that spacings above 4 would see the highest output, due to full vortex shedding from each cylinder. The range in which $L/D = 3.3$ was expected to be intermediate, as this range would have bistability between combined and individual vortex streets.

Finding the highest power at $f_s/f_n = 1.6$ was unusual, do to the fact that higher non-dimensional power was expected to occur at or near resonance. Power was expected to increase as velocity, and frequency ratio, increased, until it was eventually higher that at resonance, but the conversion to dimensionless power was expected to resolve this. It is believed that one explanation for this

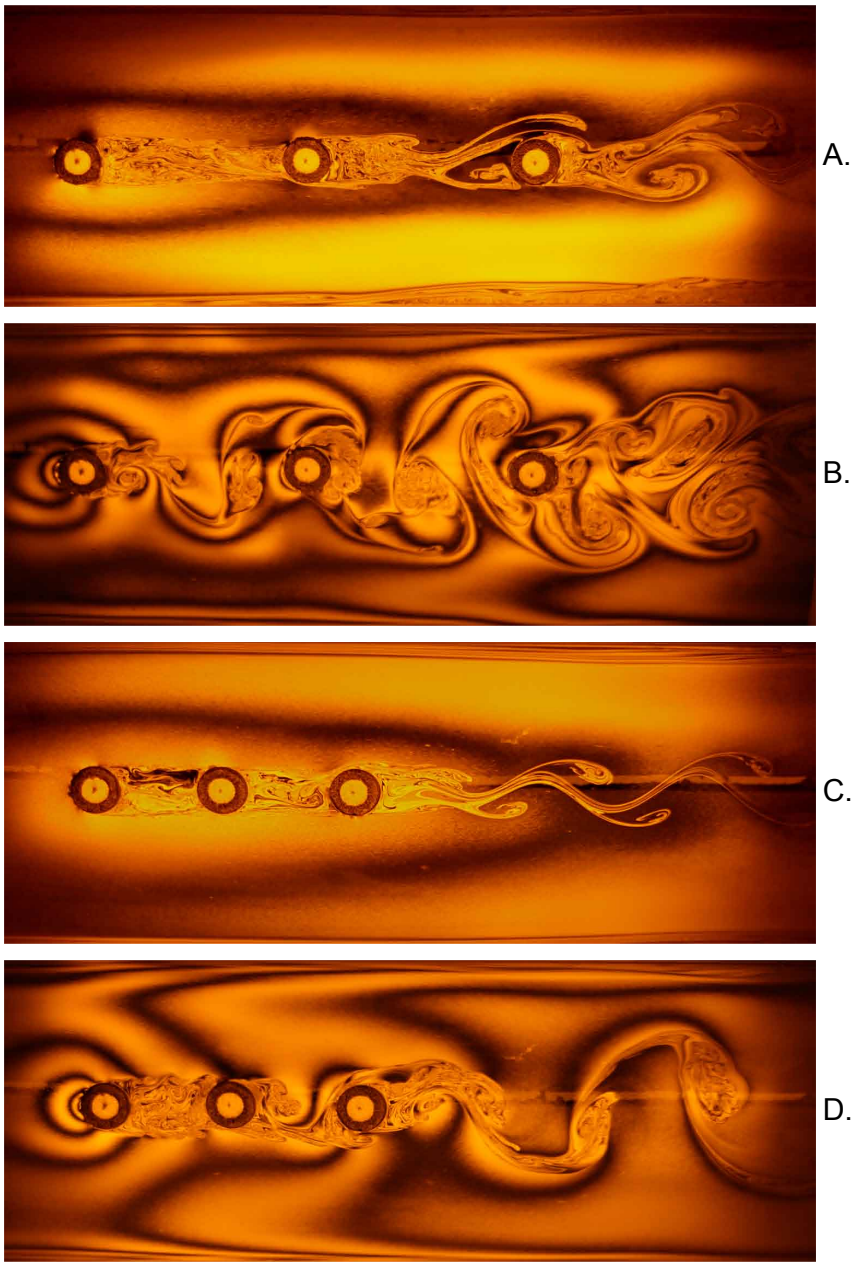

Figure 38: Flow around three cylinders at four different combinations of f_s/f_n and L/D in a soap film tunnel dimensionally matched to the piezo system. **A**: $f_s/f_n = 0.5$, $L/D = 5$; **B**: $f_s/f_n = 1.5$, $L/D = 5$; **C**: $f_s/f_n = 0.5$, $L/D = 2.5$; **D**: $f_s/f_n = 1.5$, $L/D = 2.5$. Flow is from top to bottom. For length scale reference, the width of each flow area shown is 10 cm.

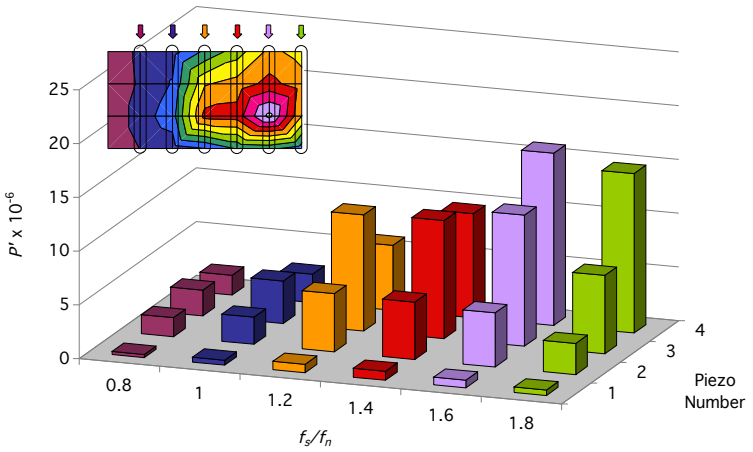

Figure 39: Dimensionless power for each individual piezo, averaged across all spacings for each frequency ratio. Subplot in the top left, corresponding to Figure 37, highlights the groups of data that were averaged to obtain each row of values. Piezos are numbered according to the diagram in Figure 35.

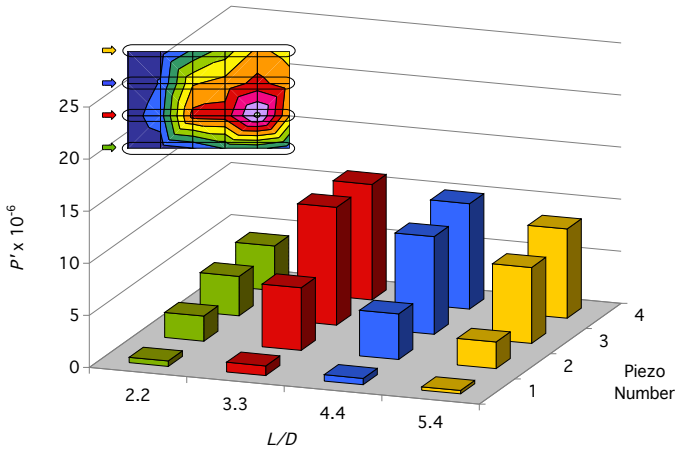

Figure 40: Dimensionless power for each individual piezo, averaged across all frequency ratios for each spacing. Subplot in the top left, corresponding to Figure 37, highlights the groups of data that were averaged to obtain each row of values.

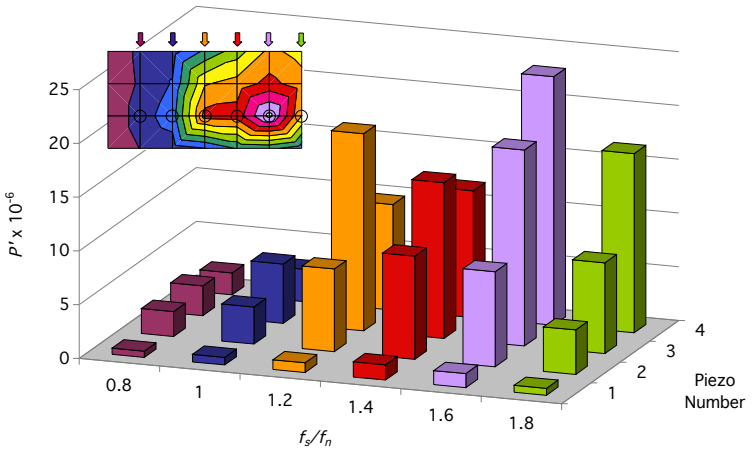

Figure 41: Dimensionless power for each individual piezo at L/D=3.3.

revolves around assumptions with the shedding frequency. First, it was assumed that the shedding frequency for the oscillating cylinders would be the same as that of stationary cylinders, ignoring the possibility of frequency lock-in. Second, it was assumed that frequency shedding would only occur in the horizontal plane. As the aspect ratio of the cylinders was fairly low, this may have been to great of an assumption.

Interesting conclusions can be drawn by comparing the flow visualization in Figure 38 with the data in Figure 37. Conditions **A** and **C** correspond to relatively low power output, while **B** and **D** are significantly higher, with **B** being slightly higher than **D**. The one possible explanation for this can bee seen in the flow structures in Figure 38, by comparing the point in the row at which vortices are first shed. In images**A**and **C**, full vortices are not formed until after the last cylinder, while in the higher-power conditions in **D** they are clearly formed after the second cylinder, and in **B** they are formed after the first cylinder, resulting an even higher power output.

CHAPTER VIII

PLANTS IN WIND

In this chapter, we cover the various aspects of our research that have involved plants. The original inspiration for our energy harvesting devices was wheat moving in the wind, and our early thinking is covered hear. Soon after the first iteration of our design, the focus of our work turned to other aspects of the design, such as testing piezos and different sails, as shown in Chapter 4. Later in the project, the focus turned back to plants, with an investigation into the effects of vortex induced vibrations on plants being started.

8.1 Early work with Plants

Plants, being sessile, have been optimized to withstand harsh hydro and aerodynamic forces [33], largely through flexibility [1]. We began by building a prototype that demonstrates the same fundamental sequence of motion as a stalk of wheat or grass. The design utilizes a thin piezoelectric transducer attached to the base of a wooden rod, with a sail at the end of the rod. In steady flow, a single period of motion of a stalk of wheat, and similarly this device, can be broken down into four phases, as shown in Figure 42. In the first phase, the object begins statically and drag force is applied, causing the stalk to bend. As the stalk moves beyond vertical in the second phase, elastic energy is stored in the bending wheat and a point is reached at which the drag and elastic forces are in equilibrium and motion comes to a stop, marking the third phase. At this point, the wheat is unstable, due to the high elastic energy stored. Any decrease in drag force due to air disturbances, such as vortices, shedding of upwind wheat, will cause the wheat to spring forward in phase four. Any losses to the kinetic energy, whether it is by friction or conversion to electricity in phases two and four, are replaced by energy from the wind in phase two.

One approach to optimization of the design that we considered was based on a modified Cauchy number, Ca, the ratio of drag and elastic forces on an object. This is shown in Equation 15,

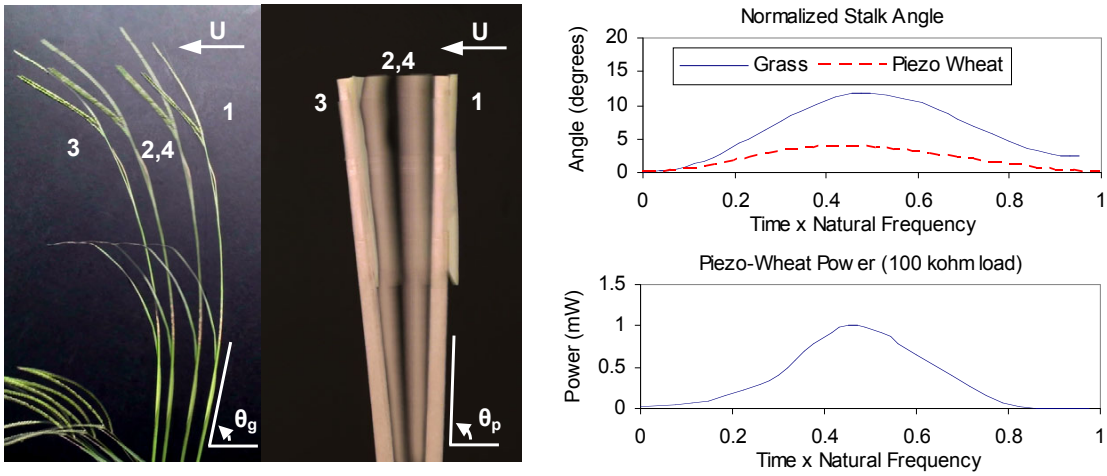

Figure 42: Phases of motion and normalized angle of rotation for grass and Piezo-Wheat in wind.

$$Ca = \frac{\rho_f U^2}{E} S^3 \tag{15}$$

where ρ_f and U are the density and velocity of the fluid, E is the elastic modulus of the object, and S is the slenderness of the object. Slenderness is the ratio of the length to the radius, as mentioned by de Langre [10]. The addition of the slenderness to the Cauchy number is not standard, but is done as the deformation of a beam is proportional to the slenderness cubed [33]. The desired value for the Cauchy number would be one, indicating a balance between elastic and drag forces, resulting in optimal resonance. Significant work has been done by others in characterizing the behavior of slender plant structures in wind, emphasizing both the fluid-body interactions [10, 12] and mechanics of the plant strength [11]. A more general study of the drag characteristics of flexible bodies has also been performed by Alben, et al. [1].Influences on a single iteration of the design due to the mechanisms of vortex and turbulence induced vibrations as well as phenomenon such as flutter and galloping [6] were to be investigated and modeled. Future work was planned to also focus theoretically and experimentally on the wake interactions of multiple devices in proximity to each other, similar to the work done by Py et al [40], in order to optimize a final product with large enough power output to be used for charging and powering remote electronic devices. Work in these areas is covered in Chapters 7 and 6.

8.2 Effects of VIV on Plants

After finding that vortex shedding in a row of elastic cylinders can increase oscillation amplitude (Chapters 7 and 6) we began to wonder if the same phenomenon could occur in plants. We found qualitative data, through word-of-mouth conversations with people familiar with forestry and agriculture, that trees several rows deep in an orchard or forest are often observed to be damaged in storms, even though the front row may not be damaged. One possible explanation for this could be vortex shedding in the wake of the first trees causing large amplitude oscillations in the latter trees, leading to damage.

Supporting our theory was work done by Shindler [47], where experiments were performed recording the displacement of trees and corresponding wind speeds. Wind data was analyzed with Fourier and wavelet transforms, and compared with the tree displacement. It was found that the largest tree oscillations occurred when large flow structures were combined with short gusts that were in the range of the natural frequency of the tree. And possibly supporting the word-of-mouth data regarding tree damage occurring after the first row was data from work by Gardiner [13]. While there was little information published about the direction of the bending moments, Gardiner showed experimental results where the mean bending moment increased by almost 20% in a middle row of trees from the front row.

Research by Whitehead found that plants subjected to constant winds can respond similarly to those in dry conditions, with increased root mass and deceased shoot and leaf area [54]. It has also been shown, as found by Niklas [34] and supported by de Langre [10], that mechanically vibrated plants will grow shorter and thicker. We planned to test plants subjected to a combination of wind and vibration through VIV.

8.2.1 Methods

To begin testing, we designed a series of experiments to get a basic look at the effects of VIV on plants. Pea plants were selected due to their fast growth rate and straight, slender stalk which could most easily be modeled as a cylinder. Plants were grown six at a time, each in individual cups. A small wind tunnel was used to grow the plants in (details of the wind tunnel are provided in Section 7.1), and fluorescent lamps were added to the roof of the lamp to provide consistent

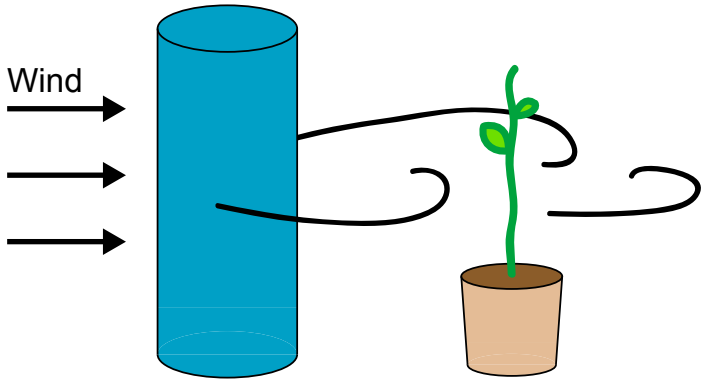

Figure 43: Layout of a plant grown behind a cylinder in wind for the VIV condition.

lighting. The planned experiments included one group of plants to be grown in the tunnel with no wind, one with unobstructed wind, and one with wind flowing around upstream cylinders. A diagram showing the location of the cylinders rekative to the plants is shown in Figure 43. The cylinders were sized to approximately a 6 cm diameter, so that the frequency of vortex shedding around the cylinders would be about 10 Hz for the windspeed used, which was 3 m/s. This was chosen because the natural frequency of a pea plant about 6 cm tall was found experimentally to be about 10 Hz. We believed that vortex shedding at or near the resonant frequency of the plant would cause the largest possible oscillations. Seeds were planted and watered, and then six days later placed in the wind tunnel. They were left in the tunnel in their respective condition, with the grow lights on, for three days. Each group was then removed, and left in the lab for three more days. At the end of these tests, the stalk height, weight, and diameter was to be measured, and the root mass was to be measured as well. All groups were watered equally at the same time intervals.

8.2.2 Results & Discussion

At the time of writing this thesis, only initial runs of the three conditions had been tested, and only three or four of the six plants in each group actually grew. The completed tests were the condition of no wind, the condition of wind with no cylinder obstruction, and the condition of wind with a cylinder obstruction. The resulting mean and standard deviation of the measurements from each test are shown in Table 3.

Although there is not enough data to confidently rule out natural variation in the plants, it does appear that some of the expected results have been observed. The root weight increases from the

Table 3: Average measurements for pea plants grown without wind, with 3 m/s wind, and with 3 m/s wind and upstream vortices.

	No Wind Mean ±Std. Dev.	Wind Mean ±Std. Dev.	VIV Wind Mean ±Std. Dev.
Initial Height (mm)	50 ±30	190 ±20	70 ±50
Final Height (mm)	250±90	300 ±20	320 ±90
ΔHeight (mm)	**200 ±70**	**105 ±37**	**250 ±50**
Stem Dia. (mm)	2.5 ±0.2	2.4 ±0.6	0.9 ±0.2
Stem Weight (g)	0.6 ±0.2	0.8 ±0.3	0.9 ±0.1
Root Weight (g)	**0.9 ±0.2**	**1.6 ±0.1**	**2.3 ±.2**

test with no wind to that of wind, and then increases again when cylinders are added. Also, the total change in height decreases with the addition of wind, but then increases again as cylinders are added. This increase was not expected, but as the deviations in the data are large, we believe that natural variation is the cause of the unexpected results.

Work is ongoing with this portion of the project, and results are expected to be submitted for publication in May of 2010. Testing will be repeated at each condition with larger numbers of plants to increase the confidence of the results.

CHAPTER IX

CONCLUDING REMARKS

9.1 Conclusions

We have reported the results of a dominantly experimental study of vortex induced vibrations in plants, a soap film system, and our novel piezoelectric energy harvesting devices. In Section 1.6, we presented a design for a remote sensing application for which our energy harvesting devices could provide power. This remote system could log air temperature and reserve power levels, and once daily would transmit data to a computer up to 100 m away. Used for demonstration purposes, this design could also be scaled up such that a network of these sensors could each individually be powered by our devices, and data could be relayed between them, increasing the effective range. Our devices were not developed to the point that this demonstration could be built, but we discussed the feasibility of this and the power requirement issues involved.

In Chapter 4, we presented the results of experiments that tested different variations on our original piezoelectric energy harvester designs, as well as characterized the relationship between the motion of our devices and the power output. These early tests dealt with the geometry of our flat sail design, and the orientation of our device relative to the wind. It was shown that sail shape had a significant influence on the performance. We also found that allowing oscillation perpendicular to the flow was more effective than parallel, which was counter to our original thinking. Power output was shown to be a function of angular velocity, which gave us a better understanding of the system and allowed our experimental process to be improved.

In Chapter 5, we developed a performance metric for our device, with which modeling and optimization could be performed. In reaching this goal, we also developed a parametric 3D CAD model which could be used to rapid prototype new designs for our devices in a 3D printing machine. Our performance model was based on vortex shedding of a single device being the driving force for power generation, and the performance metric was based on how close the design would be to resonance in a given flow. While the model had shortcomings due to assumptions made, it was an

effective starting point for a possible more advanced model.

In Chapter 6, we described the apparatus of our flow visualization system and presented qualitative and quantitative results from testing in it. The soap film tunnel we used was standard, with the exception of our method of controlling flow speed. We developed a new system of film velocity regulation using a rotameter, which we demonstrated to be effective for our uses, while being one or two orders of magnitude less expensive than common alternatives. We measured the oscillations of suspended disks in the film, which were dimensionally matched to our wind tunnel system. For some test conditions, results were in agreement with the wind tunnel system, but issues arose in repeatability for some conditions, which we discussed.

In Chapter 7, we conducted extensive experiments on the influence of spacing and flow velocity on dimensionless power output for a design of ours that included four devices in a row. We characterized the design based on a group of dimensionless parameters, and defined a simplified equation for its power output. We found that the dimensionless peak power occurred at a flow velocity higher than expected. We also found that, for each test condition, the peak power occurred at the third or fourth device in the row, indicating the wake effects from upstream devices had significant effect. We presented flow visualization from a dimensionally matched system, and discussed the insight that it provided into the behavior of our devices.

In Chapter 8, we explained the inspiration for this project, which was to develop an energy harvesting technology based on plant design. We described the fundamental steps of an object swaying in the wind, and the force balance in involved. Experiments were conducted to increase the understanding of how wind effects plants. These experiments are ongoing, with a paper being planned for submission in May of 2010 for publication.

9.2 Discussion

While our original focus on plants in wind did not stay the main driving force for this project, there were still interesting results obtained from that work. And there is still more work that can be done in the area of vortex shedding in plants. Aside from more data from the same types of tests, there are more questions that could be answered. We approximate trees and other plants as cylinders, or at least assume that they shed vortices in a similar manner. We have also gathered

qualitative, word-of-mouth references to wind damage in trees several rows into orchards and forests, while trees on the front row remain undamaged. This is very interesting to us, as it could be evidence of leading rows conditioning flow such that more oscillation occurs in later rows, similar to our cylinder arrangements. As the forestry industry has a fundamentally different focus from engineering research, obtaining data on this possible phenomenon which was useful to us proved difficult, but this is a possible area of future work.

In regards to our design testing and modeling work, we progressed substantially, but there are still questions that can be answered. Can our model from Chapter 5 be improved, especially with the dimensional analysis performed in Chapter 7? If this model can be validated, can it be effectively used for optimization? Could traditional CFD be used for modeling and optimization? Design testing stopped early in the project, and a single design was selected for testing of fundamental processes. With the knowledge gained from the testing in Chapter 7, a new design might be tuned to hit resonance at higher wind speeds, as these were shown to have higher power, even in the dimensionless form.

We made significant advances with the data we collected from spacing and velocity tests in Chapter 7, but our work was only with a single row. The effects of multiple rows can be investigated. Also, what happens when a fifth device is added? For some spacings and velocities, power dropped from the third to the fourth device. While we think a loss in the total energy in the flow may have been involved, we are not sure, and further testing could shed light on this.

Experiments could continue in the soap film, expanding the range of spacings and frequency ratios tested. A more time efficient method could be developed for gathering data from the soap film system, possibly utilizing ultrasonic or laser range finders to collect position data for the cylinders, without the need for excessive post-experiment processing. Also, testing could expand into multiple rows of cylinders, providing results that could be unique for experimental VIV research.

While much of the focus in this project was on the fundamentals of VIV, it was all built around an energy harvesting system. As discussed in Chapter 1.6, our design is almost ready for for a demonstration of a remote sensing application. Weatherproofing of our devices would be required, but the difficulty of this task would be limited. The directionality of our design would be an issue, and one solution could be to add a second piezo transducer to each device, oriented in such a way to

add a second degree of freedom. This would allow our device to oscillate in any direction. Clusters could be arranged such that devices in the middle of a group would always be in the wake of outer devices, regardless of the wind direction.

APPENDIX A

MATLAB MODELING

A.1 Piezoelectric Buzzer

A rendering of the 3D model of the piezoelectric buzzer is shown in Figure 44. The piezoelectric buzzer converts the mechanical energy from bending into electrical energy through the two PZT elements on either side of a brass plate. The brass is shown in yellow, while the visible PZT element is in white (the PZT element on the other side is not visible from the shown angle). The variable parameters for the piezo buzzer include the widths and radii of the brass and PZT, as well as their thicknesses. Because the piezo buzzer is currently a purchased part, these parameters were lower level and never changed for this project.

A.2 Pegs

A close-up of one of the pegs is shown in Figure 45. The purpose of the pegs was to connect the piezo to the ground or fixed substrate at the bottom, and the rest of the device at the top. The best method of attachment is currently a stiff adhesive such as epoxy.

The variable parameters for the peg, which are all lower level and changed from inside scripts and functions, include the length (along the z-axis), the radius, and the groove width and depth. The width of the groove is controlled by the total thickness of the piezoelectric buzzer.

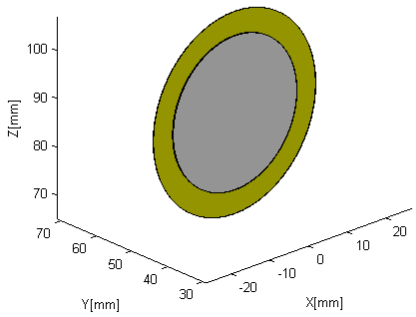

Figure 44: Matlab model of the piezoelectric buzzer.

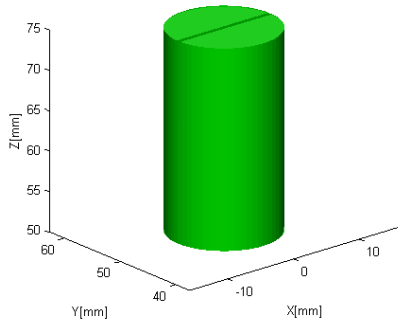

Figure 45: Close-up of the 3D geometric model of a peg.

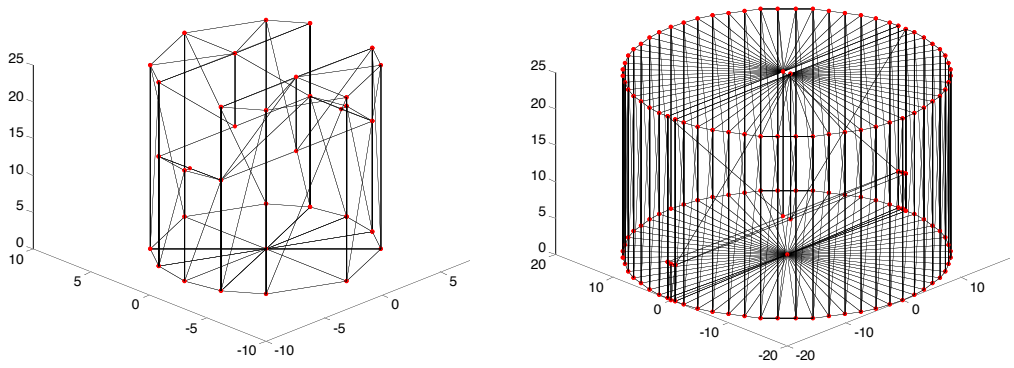

Figure 46: Wireframe view of peg vertices and faces. Right image demonstrates how vertices and faces update with changes in dimensional and resolution parameters

The peg was modeled as a cylinder, with the top edge vertices moved down to the bottom of the groove where necessary, and extra vertices were added to make the sides of the groove, and for triangulating the end surfaces. Figure 46 show the points and how they were connected to make triangular faces. The two images in Figure 46 demonstrate the parameterization of the part, as the resolution, piezo thickness, and groove depth were all changed and the part was regenerated.

A series of surf2patch() functions and loops manually labeling vertices and faces for patches were similarly created for all of the following parts for the geometric model.

A.3 Stem

The stem was designed primarily for stiffness, assuming the structure of the sail might not be rigid enough for the design. It connects the tope spacer to the bottom spacer and adjoined peg. It is not shown, is it was a simple cylinder.

The variables for the stem dimensions included the length and radius. For the purposes of this

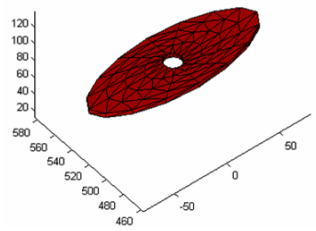

Figure 47: Close-up of the 3D geometric model of a spacer.

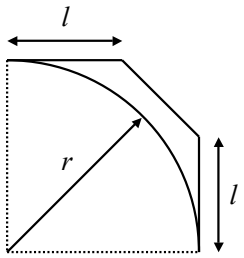

Figure 48: Control vertices locations for circle approximation.

project, the stem was always modeled, and with the same radius. More detailed analysis could find the stem unnecessary if the sail is stiff enough.

A.4 Spacers

The spacers closed off the ends of the sail, and attached it to the peg and stem. They would also add rigidity to the shape of the sail. One of the spacers is shown in Figure 47.

The variables for the spacer geometry included the width (the longest dimension in Figure 47), the depth and the thickness. The radius of the central hole was controlled directly by the radius of the stem. Variability in the thickness was added as a way to change the mass without changing any external dimensions of the Piezo-Wheat.

The spacer was modeled in a single quadrant, and then reflected to the other 3. It was made from two lofted Bezier curves, with the inside curve being the approximation of a circle using the equation $l{=}r{\times}\kappa$ to define the position of the control vertices, where $\kappa = 0.55228$ and r and l are as defined in Figure 48.

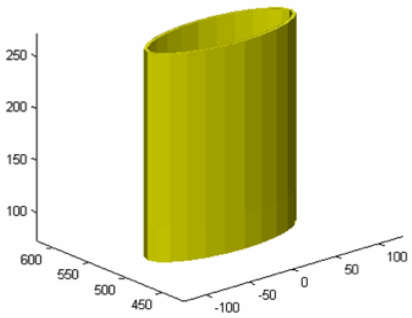

Figure 49: Close-up of the 3D geometric model of the sail.

A.5 Sail

The sail is the dominant component of the design, having the most surface area for wind interaction and having the potential to have the most mass. It is shown in Figure 49. The sail is rendered here as opaque, but is transparent in most other images to allow visualization of underlying parts.

Variable dimensions of the sail include the length, width, depth and thickness. The length is controlled by the top-level parameter of stem length, and the width and depth are controlled by the top level parameters of the spacer dimensions. The thickness, which directly influences overall width and depth, as well as mass, is a top-level parameter itself.

The sail was modeled with a basic approximation of control vertices location for the outside surface, because offset Bezier curves cannot be created perfectly. Also, the sail was made of 4 3×3 Bezier surfaces, but only 3×1 surfaces were generated for this project. An example of the 3×3 functionality is shown in Figure 50.

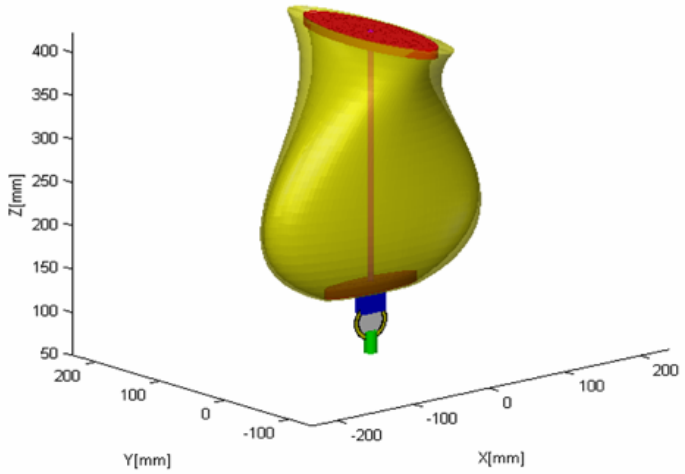

Figure 50: Example of 3×3 Bezier surface functionality in sail model.

APPENDIX B

MATLAB CODE FOR IMAGE PROCESSING

B.1 Find Coordinates of Disks

```
%find_coords_fxn.m

function [locations]=find_coords_fxn(gr,n_img,n_cir,min_d,x_max,x_min)

%Finds centroids of white ~circles greater than max_area
%Original images must be named "new001.jpg", etc., see "name" to change
%Takes ~2 seconds per frame (1200 x 600) to run
%Output is loc1, loc2, etc... with loc1 being the topmost circle, etc...
%   in (x,y) form (top left is (0,0))
%
%Set grey threshold, gr
%Set number of circles, n_cir
%Set min diameter, min_d, (pixels) of circles

min_area=pi*(min_d/2)^2;
a_err=0.05;
xy_err=0.1;

locations=zeros(n_img,2*n_cir);

for i=1:n_img;
    obj_list=0; %Reset list
    %leading zeroes for naming
    if i<10
        zer='00';
    elseif (i>=10) & (i<100)
        zer='0';
    elseif i>=100
        zer='';
    end

    name=strcat('new',zer,num2str(i),'.jpg');
    img=imread(name); %read image
    img=img(:,x_min:x_max); %crop to save time
    %smoothing - reduces time by up to 66%
    g=fspecial('gaussian',[9 9],5); %9x9, sigma=5
    img2=imfilter(img,g); %apply gaussian filter - smoothing

    bw=im2bw(img2,gr); %convert to binary image (black or white)
    bw=flipud(bw'); %rot image ccw so loc1, etc., is in (x,y) form

    %stats = regionprops(bwlabel(bw),'Area','BoundingBox',...
    stats = regionprops(bw,'Area','BoundingBox',...
        'Centroid','ConvexArea'); %find centroids
```

```
        obj_area = [stats.Area];
        count_a=1;
        for j=1:length(stats)
            if obj_area(j) < min_area %if object is too small, continue
                continue
            end

            obj_conv_a = stats(j).ConvexArea;
            obj_x_width = stats(j).BoundingBox(3);
            obj_y_width = stats(j).BoundingBox(4);
            obj_d_equiv = 2*sqrt(obj_area(j)/pi); %dia of circle w/ same area

            obj_x_pos = stats(j).Centroid(2);

            area_error = abs(obj_area(j) - obj_conv_a) / obj_conv_a;
            x_error = abs(obj_x_width - obj_d_equiv) / obj_d_equiv;
            y_error = abs(obj_y_width - obj_d_equiv) / obj_d_equiv;

            if area_error < a_err & x_error < xy_err & y_error < xy_err
                obj_list(count_a)=j; %List of objects that meet criteria
                count_a=count_a+1;
            end
        end

%Remove objects from BW List that do not meet criteria
        L=bwlabel(bw);
        count_b=1;
        for k=1:length(stats)
            if any(obj_list==k)
                L(L==k)=count_b; %Renumbers objects to 1,2,...
                count_b=count_b+1;
            else
                L(L==k)=0;
            end
        end

    stats_reduced = regionprops(L, 'centroid'); %find centroids
    %save centroid coordinates
    loc_temp = cat(2, stats_reduced.Centroid);
    locations(i,1:length(loc_temp))=loc_temp;
end
end
```

Bibliography

[1] Alben, S., Shelley, M., and Zhang, J., "Drag reduction through self-similar bending of a flexible body," *Nature*, vol. 420, no. 6915, pp. 479–481, 2002.

[2] Allen, D. and Henning, D., "Vortex-induced vibration current tank tests of two equal-diameter cylinders in tandem," *Journal of Fluids and Structures*, vol. 17, no. 6, pp. 767–781, 2003.

[3] Bearman, P., "Vortex shedding from oscillating bluff bodies," *Annual Review of Fluid Mechanics*, vol. 16, no. 1, pp. 195–222, 1984.

[4] Beizaie, M. and Gharib, M., "Fundamentals of a liquid (soap) film tunnel," *Experiments in Fluids*, vol. 23, no. 2, pp. 130–140, 1997.

[5] Bernitsas, M. M., Raghavan, K., Ben-Simon, Y., and Garcia, E. M. H., "Vivace (vortex induced vibration aquatic clean energy): A new concept in generation of clean and renewable energy from fluid flow," *Journal of Offshore Mechanics and Arctic Engineering-Transactions of the Asme*, vol. 130, no. 4, 2008.

[6] Blevins, R. D., *Flow-induced vibration*. New York: Van Nostrand Reinhold, 2nd ed., 1990.

[7] Couder, Y. and Basdevant, C., "Experimental and numerical study of vortex couples in two-dimensional flows," *Journal of Fluid Mechanics*, vol. 173, pp. 225–251, 1986.

[8] Couder, Y., Chomaz, J., and Rabaud, M., "On the hydrodynamics of soap films," *Physica D*, vol. 37, no. 1-3, pp. 384–405, 1989.

[9] Cymbet Corporation, "EnerChip EH CBC5300 Energy Harvesting Module," http://www.cymbet.com/MContentA/pdfs/DS-72-06.pdf, 2009, Accessed March 2010.

[10] de Langre, E., "Effects of wind on plants," *Annual Review of Fluid Mechanics*, vol. 40, pp. 141–168, 2008.

[11] Farquhar, T. and Meyer-Phillips, H., "Relative safety factors against global buckling, anchorage rotation, and tissue rupture in wheat," *Journal of Theoretical Biology*, vol. 211, no. 1, pp. 55–65, 2001.

[12] Farquhar, T., Wood, J. Z., and van Beem, J., "The kinematics of wheat struck by a wind gust," *Journal of Applied Mechanics-Transactions of the Asme*, vol. 67, no. 3, pp. 496–502, 2000.

[13] Gardiner, B. A., Stacey, G. R., Belcher, R. E., and Wood, C. J., "Field and wind tunnel assessments of the implications of respacing and thinning for tree stability," *Forestry*, vol. 70, no. 3, pp. 233–252, 1997.

[14] Gaydon, M. and Rockwell, D., "Vortices incident upon an oscillating cylinder: Flow structure and loading," *Journal of Fluids and Structures*, vol. 13, no. 6, pp. 709–722, 1999.

[15] Gharib, M. and Derango, P., "A liquid film (soap film) tunnel to study two-dimensional laminar and turbulent shear flows," *Physica D Nonlinear Phenomena*, vol. 37, pp. 406–416, 1989.

[16] Goldfarb, M. and Jones, L. D., "On the efficiency of electric power generation with piezoelectric ceramic," *Journal of Dynamic Systems Measurement and Control-Transactions of the Asme*, vol. 121, no. 3, pp. 566–571, 1999.

[17] Govardhan, R. and Williamson, C. H. K., "Critical mass in vortex-induced vibration of a cylinder," *European Journal of Mechanics B-Fluids*, vol. 23, no. 1, pp. 17–27, 2004.

[18] Hetz, A., Dhaubhadel, M., and Telionis, D., "Vortex shedding over five in-line cylinders," *Journal of Fluids and Structures*, vol. 5, pp. 243–257, 1991.

[19] Igarashi, T., "Characteristics of the flow around 4 circular-cylinders arranged in line," *Bulletin of the Jsme-Japan Society of Mechanical Engineers*, vol. 29, no. 249, pp. 751–757, 1986.

[20] Igarashi, T. and Suzuki, K., "Characteristics of the flow around 3 circular-cylinders arranged in line," *Bulletin of the Jsme-Japan Society of Mechanical Engineers*, vol. 27, no. 233, pp. 2397–2404, 1984.

[21] Jauvtis, N. and Williamson, C. H. K., "The effect of two degrees of freedom on vortex-induced vibration at low mass and damping," *Journal of Fluid Mechanics*, vol. 509, pp. 23–62, 2004.

[22] Kellay, H., Wu, X., and Goldburg, W., "Experiments with turbulent soap films," *Physical Review Letters*, vol. 74, no. 20, pp. 3975–3978, 1995.

[23] Khalak, A. and Williamson, C., "Motions, forces and mode transitions in vortex-induced vibrations at low mass-damping," *Journal of Fluids and Structures*, vol. 13, no. 7-8, pp. 813–851, 1999.

[24] Lam, K. and Cheung, W., "Phenomena of vortex shedding and flow interference of three cylinders in different equilateral arrangements," *Journal of Fluid Mechanics*, vol. 196, pp. 1–26, 1988.

[25] Lin, J. C., Yang, Y., and Rockwell, D., "Flow past two cylinders in tandem: Instantaneous and averaged flow structure," *Journal of Fluids and Structures*, vol. 16, no. 8, pp. 1059–1071, 2002.

[26] Mahir, N. and Rockwell, D., "Vortex formation from a forced system of two cylinders .1. tandem arrangement," *Journal of Fluids and Structures*, vol. 10, no. 5, p. 473, 1996.

[27] Mahir, N. and Rockwell, D., "Vortex formation from a forced system of two cylinders .2. side-by-side arrangement," *Journal of Fluids and Structures*, vol. 10, no. 5, p. 491, 1996.

[28] Martin, B., "Shear flow in a two dimensional couette cell: A technique for measuring the viscosity of free standing liquid films," *Review of Scientific Instruments*, vol. 66, p. 5603, 1995.

[29] Mittal, S. and Kumar, V., "Flow-induced oscillations of two cylinders in tandem and staggered arrangements," *Journal of Fluids and Structures*, vol. 15, no. 5, pp. 717–736, 2001.

[30] Mittal, S. and Kumar, V., "Vortex induced vibrations of a pair of cylinders at reynolds number 1000," *International Journal of Computational Fluid Dynamics*, vol. 18, no. 7, pp. 601–614, 2004.

[31] Mizushima, J. and Suehiro, N., "Instability and transition of flow past two tandem circular cylinders," *Physics of Fluids*, vol. 17, no. 10, 2005.

[32] Myers, R., Vickers, M., Kim, H., and Priya, S., "Small scale windmill," *Applied Physics Letters*, vol. 90, no. 5, pp. –, 2007.

[33] Niklas, K. J., *Plant biomechanics : an engineering approach to plant form and function.* Chicago: University of Chicago Press, 1992.

[34] Niklas, K., "Effects of vibration on mechanical properties and biomass allocation pattern ofcapsella bursa-pastoris (cruciferae)," *Annals of Botany*, vol. 82, no. 2, p. 147, 1998.

[35] Platt, S. R., Farritor, S., and Haider, H., "On low-frequency electric power generation with pzt ceramics," *Ieee-Asme Transactions on Mechatronics*, vol. 10, no. 2, pp. 240–252, 2005.

[36] Priya, S., "Modeling of electric energy harvesting using piezoelectric windmill," *Applied Physics Letters*, vol. 87, no. 18, 2005.

[37] Priya, S., "Advances in energy harvesting using low profile piezoelectric transducers," *Journal of Electroceramics*, vol. 19, no. 1, pp. 165–182, 2007.

[38] Priya, S., Chen, C. T., Fye, D., and Zahnd, J., "Piezoelectric windmill: A novel solution to remote sensing," *Japanese Journal of Applied Physics Part 2-Letters & Express Letters*, vol. 44, no. 1-7, pp. L104–L107, 2005.

[39] Priya, S., Taneja, R., Myers, R., and Islam, R., "Piezoelectric energy harvesting using bulk transducers," in *Piezoelectric and Acoustic Materials for Transducer Applications* (Safari, A. and Akdoan, E. K., eds.), pp. 373–388, Springer US, 2008.

[40] Py, C., de Langre, E., and Moulia, B., "A frequency lock-in mechanism in the interaction between wind and crop canopies," *Journal of Fluid Mechanics*, vol. 568, pp. 425–449, 2006.

[41] Ristroph, L. and Zhang, J., "Anomalous hydrodynamic drafting of interacting flapping flags," *Physical Review Letters*, vol. 101, no. 19, p. 194502, 2008.

[42] Rivera, M., Belmonte, A., Goldburg, W., Wu, X., and Kellay, H., "Optical fiber velocimetry: A technique for measuring velocity in two-dimensional flows," *Review of Scientific Instruments*, vol. 69, p. 3215, 1998.

[43] Rockwell, D., "Vortex-body interactions," *Annual Review of Fluid Mechanics*, vol. 30, pp. 199–229, 1998.

[44] Rutgers, M., Bhagavatula, R., Petersen, A., and Goldburg, W., "Two dimensional velocity profiles and laminar boundary layers in flowing soap films," *Physics of Fluids*, vol. 8, p. 2847, 1996.

[45] Rutgers, M., Wu, X., and Daniel, W., "Conducting fluid dynamics experiments with vertically falling soap films," *Review of Scientific Instruments*, vol. 72, p. 3025, 2001.

[46] Schmidt, V., "Piezoelectric energy conversion in windmills," *IEEE 1992 Ultrasonics Symposium Proceedings*, vol. 2, pp. 897–904, 1992.

[47] Shindler, D., "Responses of scots pine trees to dynamic wind loading," *Agricultural and Forest Meteorology*, vol. 148, no. 11, pp. 1733–1742, 2008.

[48] Sodano, H. A., Inman, D. J., and Park, G., "Comparison of piezoelectric energy harvesting devices for recharging batteries," *Journal of Intelligent Material Systems and Structures*, vol. 16, no. 10, pp. 799–807, 2005.

[49] Sodano, H., Park, G., and Inman, D., "Estimation of electric charge output for piezoelectric energy harvesting," *Strain*, vol. 40, no. 2, pp. 49–58, 2004.

[50] Tanida, Y., Okajima, A., and Watanabe, Y., "Stability of a circular-cylinder oscillating in uniform-flow or in a wake," *Journal of Fluid Mechanics*, vol. 61, no. DEC18, pp. 769–784, 1973.

[51] Tatsuno, M., Amamoto, H., and Ishi-i, K., "Effects of interference among three equidistantly arranged cylinders in a uniform flow," *Fluid Dynamics Research*, vol. 22, pp. 297–315, 1998.

[52] Taylor, G. W., Burns, J. R., Kammann, S. M., Powers, W. B., and Welsh, T. R., "The energy harvesting eel: A small subsurface ocean/river power generator," *Ieee Journal of Oceanic Engineering*, vol. 26, no. 4, pp. 539–547, 2001.

[53] Texas Instruments, Inc., "eZ430-Chronos Development Tool User's Guide, SLAU292," http://focus.ti.com/lit/ug/slau292/slau292.pdf, 2009, Accessed March 2010.

[54] Whitehead, F. and Luti, R., "Experimental studies of the effect of wind on plant growth and anatomy. i. zea mays," *New Phytologist*, vol. 61, no. 1, pp. 56–58, 1962.

[55] Williamson, C. H. K., "Vortex dynamics in the cylinder wake," *Annual Review of Fluid Mechanics*, vol. 28, pp. 477–539, 1996.

[56] Williamson, C. H. K. and Govardhan, R., "Vortex-induced vibrations," *Annual Review of Fluid Mechanics*, vol. 36, pp. 413–455, 2004.

[57] Zdravkovich, M. M. and Pridden, D. L., "Interference between 2 circular-cylinders - series of unexpected discontinuities," *Journal of Industrial Aerodynamics*, vol. 2, no. 3, pp. 255–270, 1977.

[58] Zdravkovich, M., "The effects of interference between circular cylinders in cross flow," *Journal of Fluids and Structures*, vol. 1, no. 2, pp. 239–261, 1987.

[59] Zhang, J., Childress, S., Libchaber, A., and Shelley, M., "Flexible filaments in a flowing soap film as a model for one-dimensional flags in a two-dimensional wind," *Nature*, vol. 408, no. 6814, pp. 835–839, 2000.

[60] Zhou, C. Y., So, R. M. C., and Lam, K., "Vortex-induced vibrations of an elastic circular cylinder," *Journal of Fluids and Structures*, vol. 13, no. 2, pp. 165–189, 1999.

[61] Ziada, S. and Oengren, A., "Vortex shedding in an in-line tube bundle with large tube spacings," *Journal of Fluids and Structures*, vol. 7, pp. 661–687, 1993.